

University of New Mexico

## UNM Digital Repository

---

Mechanical Engineering ETDs

Engineering ETDs

---

Spring 4-14-2021

### Feasibility Study of a Structural Electrolyte Containment Ring for use in Thermal Batteries

Teal Harbour

*University of New Mexico - Main Campus*

Follow this and additional works at: [https://digitalrepository.unm.edu/me\\_etds](https://digitalrepository.unm.edu/me_etds)



Part of the [Mechanical Engineering Commons](#)

---

#### Recommended Citation

Harbour, Teal. "Feasibility Study of a Structural Electrolyte Containment Ring for use in Thermal Batteries." (2021). [https://digitalrepository.unm.edu/me\\_etds/206](https://digitalrepository.unm.edu/me_etds/206)

This Thesis is brought to you for free and open access by the Engineering ETDs at UNM Digital Repository. It has been accepted for inclusion in Mechanical Engineering ETDs by an authorized administrator of UNM Digital Repository. For more information, please contact [disc@unm.edu](mailto:disc@unm.edu).

Teal S. Harbour

---

*Candidate*

Mechanical Engineering

---

*Department*

This thesis is approved, and it is acceptable in quality and form for publication:

*Approved by the Thesis Committee:*

Nathan Jackson, Chairperson

---

Yu-Lin Shen

---

Eric Allcorn

---

**Feasibility Study of a Structural Electrolyte Containment Ring for use  
in Thermal Batteries**

**BY**

**Teal S. Harbour**  
**B.S. Mechanical Engineering**

THESIS

Submitted in Partial Fulfillment of the  
Requirements for the Degree of

**Master of Science**

**Mechanical Engineering**

The University of New Mexico  
Albuquerque, New Mexico

**May 2021**

## **Acknowledgements**

I would like to acknowledge my peers and mentors of the University of New Mexico and Sandia National Laboratories. I am privileged to have Dr. Nathan Jackson and Dr. Yu-Lin Shen not only as former instructors, but as members of my thesis committee. I would like to thank Chris Orendorff and Kyle Fenton for the invaluable learning experience during my internship in the Power Source and Technology Group. I'd like to thank Eric Allcorn who has been an exemplar team leader, while also sharing his wealth of knowledge. Lastly, Bertha Montoya and Ganesan Nagasubramanian have my deepest gratitude for their utmost hospitality and mentorship.

Sandia National Laboratories is a multi-mission laboratory managed and operated by National Technology and Engineering Solutions of Sandia, LLC., a wholly owned subsidiary of Honeywell International, Inc., for the U.S. Department of Energy's National Nuclear Security Administration under contract DE-NA-0003525. This paper describes objective technical results and analysis. Any subjective views or opinions that might be expressed in the paper do not necessarily represent the views of the U.S. Department of Energy or the United States Government.

# **Feasibility Study of a Structural Electrolyte Containment Ring for use in Thermal Batteries**

**by**

**Teal S. Harbour**

**B.S., Mechanical Engineering, University of New Mexico, 2019**

**M.S., Mechanical Engineering, University of New Mexico, 2021**

## **Abstract**

The feasibility of a new thermal battery separator design utilizing a structural machined MACOR<sup>®</sup> ceramic is explored. The cylindrical ceramic “separator ring” maintains separation of cell electrodes while containing a LiCl-KCl molten salt electrolyte. Finite element analysis (FEA) results show the separator ring can withstand mechanical and thermal loading conditions representative of a thermal battery environment. Electrical Impedance Spectroscopy (EIS) was used to characterize impedance mechanisms. EIS data was also used to calculate and show conductivities of the experimental separators are comparable to a traditional pellet. Although discharge testing resulted in high current-pulse resistivities and low delivered capacity, the work done in this study proves the separator ring concept as a viable option for future thermal battery development.

# Table of Contents

List of Tables .....	viii
List of Figures .....	vi
Chapter 1 Introduction .....	1
1.1 Chapter Overview .....	1
1.2 Thermal Batteries and Separators .....	1
1.3 Background and Relevant Literature .....	3
Chapter 2 Separator Design and Finite Element Analysis .....	5
2.1 Separator Design .....	5
2.2 Finite Element Modeling and Simulation .....	7
2.3 Initial Conditions and Loading .....	7
2.5 Mesh and Material Properties .....	11
2.6 Mechanical Stability .....	14
2.7 Model Theory .....	14
2.8 FEA Results .....	15
2.9 Validation .....	20
Chapter 3 Electrochemical Characterization .....	21
3.1 Material Preparation and Electrochemical Procedures .....	21
3.2 Single Cell Testing and Electrical Impedance Testing .....	22
3.3 Electrochemical Performance .....	24
3.4 Conductivity .....	24
3.5 Current-Pulse Discharge Performance .....	31
Chapter 4 Conclusion and Future Work .....	36
4.1 Conclusion and Future Work .....	36
References .....	38
Appendix .....	40
A. Electrical Impedance Data .....	40
B. Discharge Data .....	49

## List of Figures

Figure 1. Thermal Battery Schematic <sup>3</sup> .....	2
Figure 2. Representation of a thermal battery single cell in its inactive (left) and active states (right). .....	5
Figure 3. Representation of thermal battery single cell with MACOR <sup>®</sup> ceramic ring. ....	6
Figure 4. Diagram of experimental separator design.....	7
Figure 5. Prescribed axial and thermal boundary conditions.....	8
Figure 6. Prescribed axial loading. Electrolyte in solid phase with no radial force exerted. ....	9
Figure 7. Prescribed axial, radial, and thermal loading of ABAQUS model.....	9
Figure 8. Generated mesh used for ABAQUS model.....	11
Figure 9. Young's Modulus vs temperature <sup>16</sup> .....	12
Figure 10. Modulus of rupture vs temperature <sup>16</sup> .....	13
Figure 11. 3D Cylindrical Element <sup>18</sup> .....	15
Figure 12. Radial stress distribution (rr direction) at t=0.5 sec of loading step 4.....	16
Figure 13. Hoop stress distribution ( $\theta\theta$ directions) at t=0.5 sec of loading step 4.....	17
Figure 14. Axial stress distribution (zz direction) at t=0.5 sec of loading step 4. ....	18
Figure 15. Absolute stress vs temperature .....	19
Figure 16. Strain vs temperature.....	19
Figure 17. Single cell being assembled with control pellet separator (left) and experimental separator (right).....	21
Figure 18. Single cell test fixture.....	23
Figure 19. Active area (A) for traditional pellet (left) and experimental (right) separator.....	24
Figure 20. Frequency response data for control and experimental separators at 475C, 500C, and 525C. ....	25
Figure 21. Equivalent circuit for traditional MgO/LiCl-KCl pellet system.....	27
Figure 22. Equivalent circuit for experimental separator system. ....	27
Figure 23. Specific conductivity of experimental separator cells.....	29
Figure 24. Specific conductivity normalized by active area and mass. ....	30
Figure 25. Specific conductivity (normalized by active area and mass) vs active area... ..	30

Figure 26. Current-pulse voltage responses for the control and experimental (SR10, SR35) single cells at 475, 500,525C. ....	32
Figure 27. Typical discharge curve of experimental separator single cell with LiB anode and FeS2 cathode. ....	33
Figure 28. Compiled pulse resistivities for control and experimental cells at 475, 500, and 525C.....	34
Figure 29. Delivered Specific Capacity (normalized by anode mass) vs Temperature for control and experimental cells at 475, 500, and 525C.....	35

## List of Tables

Table 1. Overview of loading steps prescribed to ABAQUS model. ....	8
Table 2. Mechanical and thermal loading of ABAQUS simulation. ....	10
Table 3. Anode and cathode capacity details. ....	31

# **Chapter 1 Introduction**

## **1.1 Chapter Overview**

Chapter 1 will introduce thermal batteries, the separator component, and properties impacting its reliability and performance. In chapter 2, the experimental separator design and FEA process are presented followed by a discussion of results. Chapter 3 includes details on materials preparation and procedures used for EIS and discharge testing. Data is presented and followed by a discussion of the electrochemical performance of both control and experimental cells. Lastly, a conclusion and discussion of future work is presented in Chapter 4.

## **1.2 Thermal Batteries and Separators**

Thermal batteries are energy storage devices designed to remain inert for extended periods of time and have the ability to deliver high power discharge rates<sup>1</sup>. The battery remains inert by utilizing an electrolyte which does not become ionically active until a eutectic temperature is reached and transitions from a solid to molten liquid. Thermal batteries are typically comprised of an anode, cathode, separator, and heat source stacked in series as shown in Figure 1. These components are in the form of a pellet which have been pressed under a mechanical load from their powder constituents. The separator is a unique component in thermal batteries and serves various functions such as means for mechanical stability and ionic conductivity<sup>2</sup>.

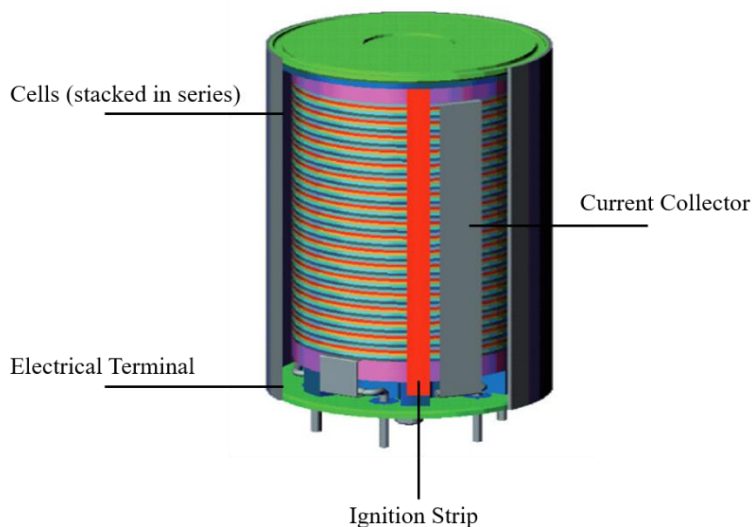


Figure 1. Thermal Battery Schematic<sup>3</sup>

A thermal battery separator is comprised of an ionically conductive salt electrolyte and binding oxide powder to immobilize it upon the solid-liquid phase transition. A common electrolyte used is the lithium chloride-potassium chloride (LiCl-KCl) binary system at which the phase transition occurs at  $352\text{ C}^1$ . Thermal batteries endure harsh environmental conditions such as acceleration, spin, shock, and vibrations<sup>2</sup>. In its molten state, the electrolyte must be retained to maintain battery performance and functionality. Magnesium Oxide (MgO) typically serves as the immobilizing agent and is added proportionally to the LiCl-KCl eutectic.

MgO is a non-conductive material therefore traditional design of a thermal battery separator is inherently a balance between mechanical stability and ionic conductivity. Variabilities in MgO include purity, surface area, particle and pore size distributions, and morphology. Particle and pore size distributions are interrelated parameters and found to be correlated with deformation<sup>5</sup>. Insufficient binder content can result in excessive deformation and electrolyte leakage. Meanwhile, excessive binder content impedes the ionic conductivity of the separator<sup>4</sup>.

Alternative binder materials have been used and explored to improve the thermal battery separator including, fiberglass tape, ceramic felts, and custom MgO films that have been back filled with electrolyte. However, incorporation of these types of materials present

new problems such as manufacturability, achieving optimal electrolyte loading, and material compatibility. Electrolyte loading of these types of binder matrix materials is typically a function of open porosity, pore size, and wettability. Studies<sup>6,7</sup> have been conducted into how these properties effect thermal battery performance at the single cell level and found alternative binder materials can produce discharge performance comparable to a traditional pellet separator.

A new thermal battery separator design will be proposed that utilizes a commercial machinable ceramic. The experimental design consists of a cylindrical “separator ring”, made of MACOR<sup>®</sup> ceramic and an all LiCl-KCl electrolyte pellet. The geometry the separator ring eliminates the need for an immobilizing binder (MgO) as it provides both separation of the electrodes and retention of the electrolyte in it molten state. The feasibility of the experimental design will be investigated via FEA with prescribed loading conditions representative of a thermal battery environment. Electrochemical performance of the separator will be characterized by EIS and discharge testing.

### **1.3 Background and Relevant Literature**

Thermal batteries are an innovative war time weapon development by the Germans during WWII. The national Bureau of Standards Ordnance Development Division (NBS-ODD) further developed this technology which was ultimately adopted by the Department of Defense (DoD). Since their development, there have been inherent problems concerning electrolyte leakage in thermal batteries<sup>8</sup>. Glass tapes and ceramic felts have been used since the early 1950’s in an attempt to solve this problem<sup>2</sup>. However, for decades it would be the thermal battery separator pellet as a pressed mixture of electrolyte and MgO that would prove to be the most utilized separator design option for its reliability and ease of manufacturability.

The evaluation of alternative materials such as glass tapes and ceramic discs back filled with electrolyte resumed in the late 1990’s. Ronald A. Guidotti and Frederick W. Reinhardt manufactured prototype separators by dipping these porous materials into molten salt electrolytes. Early studies<sup>3</sup> suggest that the performance of composite separators is severely dependent on the electrolyte loading. Material evaluations of borosilicate glass a commercial MgO coated aluminosilicate disc filled with a LiCl-KCl

electrolyte would yield similar electrochemical performances to that of a traditional pressed pellet. Although performance evaluations of these composite separators were promising, they generally exceeded the mass of traditional control pellets and mechanical stability was not deeply evaluated.

Various materials such as gelled MgO dispersions, emulsions, and ceramic foams would continue to be studied to produce a composite separator. These materials which provide mechanical support of the separator are able to be tuned to have desired porosity, tortuosity, and pore size, allowing for optimal ionic mobility of the electrolyte. However, these types of microporous materials are inherent to their own problems such as increased complexity in manufacturing and optimizing the previously mentioned properties. In a report by Mondy et al<sup>9</sup>, various microporous films are produced and loaded with electrolyte to show comparable voltage life and conductivity characteristics. For both produced gelled MgO dispersion and emulsion porous structures, fracture strength was found to be adequate for use in a thermal battery with electrical performance comparable to traditional pellet technology.

The previous investigations into the mechanical feasibility of a composite separator validate the concept. However, they do not describe the complex thermo-mechanical interactions between the phase changing electrolyte and microporous materials used to immobilize it. Long et al<sup>10</sup> would later publish a report that presents such a phenomenological constitutive model of pressed-pellet materials mechanics involving such electrolytes. These constitutive models in combination with the finite element method would bring the historical technology of thermal batteries into the era of powerful computer aided modeling and simulation capabilities. Thermally Activated Battery Simulator (TABS)<sup>11</sup> is a realization of today's modeling tools, allowing design engineers to analyze performance characteristics of experimental materials.

## Chapter 2 Separator Design and Finite Element Analysis

### 2.1 Separator Design

Thermal batteries are subjected to both mechanical and thermal loading. During manufacturing the cell stack is subjected to an axial preload ranging from 1.2 to 2.5 MPa to ensure good interfacial contact and prevent movement after the electrolyte's phase transition<sup>12</sup>. Typically, a single cell comprised of an anode, cathode, and separator is used to characterize baseline mechanical and electrochemical behavior of thermal battery components. A new separator design was motivated by observed relaxation or slumping effects during single cell testing as shown in Figure 2. In this instance MgO and Electrolyte leak radially outward, volume of the separator is not conserved, and a decrease in thickness is observed<sup>2,4</sup>.

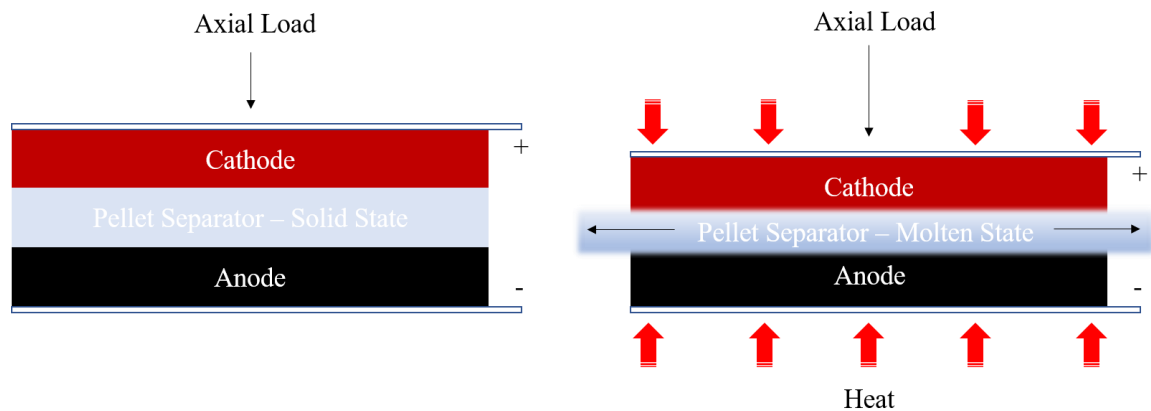


Figure 2. Representation of a thermal battery single cell in its inactive (left) and active states (right).

To address the slumping problem, a cylindrical “Separator Ring” (Figure 3.) made from a nonconductive material was proposed. The cylindrical geometry would simultaneously provide mechanical separation of the electrodes and contain the electrolyte. MgO was an initial material selection for its proven stability with molten salts at elevated temperatures<sup>2</sup>. However, initial attempts to produce prototypes were challenged by manufacturing difficulties and lead times. A ceramic material known as MACOR<sup>®</sup> was ultimately chosen for its machinability, stability at high temperatures, and ability to be electronically insulative.

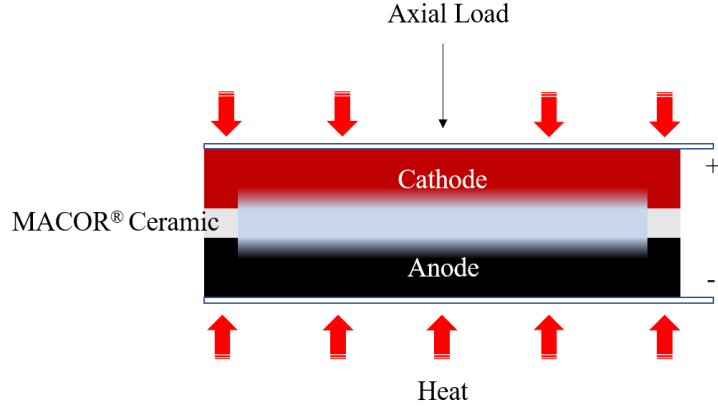


Figure 3. Representation of thermal battery single cell with MACOR® ceramic ring.

Energy storage devices strive to increase their specific energy (by mass) and energy density (by volume). It is with this concept in mind that the physical dimensions of the structural part of the separator were computed. The target mass of the MACOR® ceramic  $m_M$  was set to match the MgO content  $M_{MgO}$  in a traditional pellet with a known geometry  $V_p$ . Fixing the outer radius and thickness, the inner radius  $r$  of the separator ring was solved for using the relationship between mass, density, and volume. By computing the inner radial dimension of the separator ring based on mass percentages of MgO in a traditional separator pellet (EQN 1-4), the specific energy could be matched or exceeded for the experimental cells.

$$m_p = \rho_p V_p \quad (1)$$

$$M_{MgO} = m_M = \%MgO * m_p \quad (2)$$

$$\rho_M = \frac{m_M}{V_M}, \quad \text{where } V_M = \pi * (R^2 - r^2)t \quad (3)$$

$$r = \sqrt{R^2 - \frac{m_M}{\pi \rho_M t}} \quad (4)$$

The electrolyte to be used in combination with the separator ring was also given careful design consideration. Initial testing of single cells where the ceramic ring had simply been back filled with electrolyte powder resulted in malfunctions and incomplete tests. Alternatively, an all LiCl-KCl salt pellet had to be designed which could then be inserted

into to inner space of the separator ring. The density and volume of this pellet were chosen to allow for a void space between the pellet and separator ring. The purpose of this void space is to allow for a desired amount of an electrolytes volumetric expansion which plays a critical role in wetting the electrodes and maintaining surface contact.

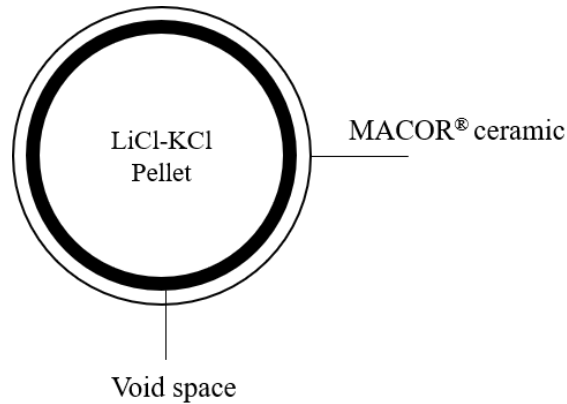


Figure 4. Diagram of experimental separator design

## 2.2 Finite Element Modeling and Simulation

To evaluate the mechanical feasibility of using a MACOR® ceramic separator ring, a finite element model representative of a thermal battery environment was built using ABAQUS. The model is divided into simplified loading steps<sup>13</sup> to solely examine the mechanical and thermal loading of the ceramic ring. The mechanical loads are represented by prescribed axial and inner radial pressures. Axial loads represent the closing force a cell experiences during manufacturing and subsequent changes during battery activation. The inner radial loading represents a force exerted due to the electrolyte's volumetric expansion. Thermal loading is prescribed uniformly and is representative of the heating process a cell undergoes to become active and maintain a voltage.

## 2.3 Initial Conditions and Loading

Initial mechanical and thermal boundary conditions were prescribed to the ABAQUS model. For a thermal battery cell with the experimental ceramic separator ring as shown in Figure 3, the contact surfaces are electrodes. These electrodes are not incorporated into the model. A displacement boundary condition was chosen for the axial Z direction (Figure 5), allowing for radial expansion. The thermal boundary condition was set to a room temperature of 25 C.

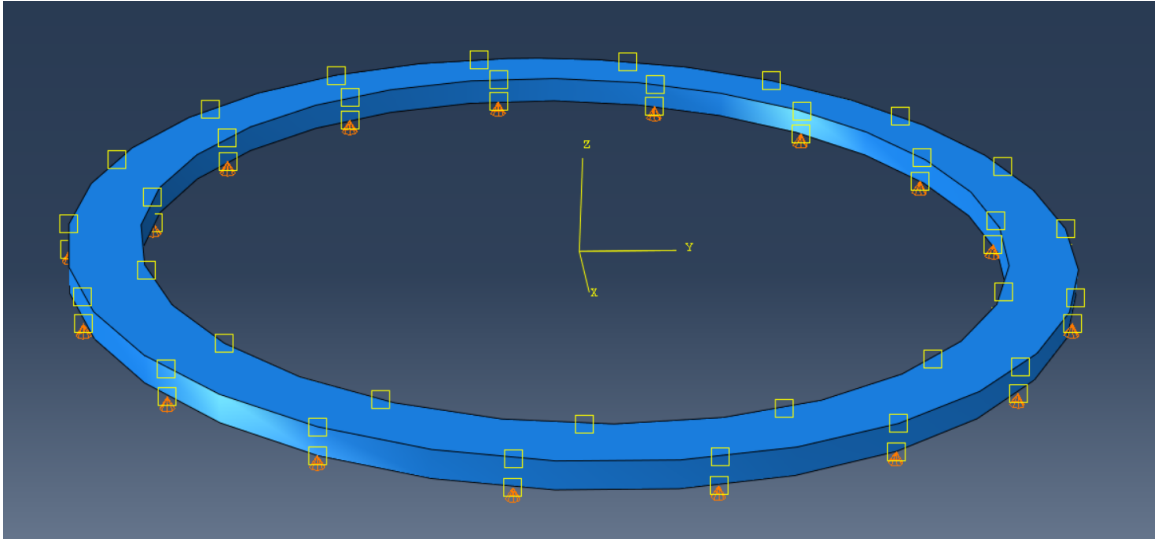


Figure 5. Prescribed axial and thermal boundary conditions.

Table 1. Overview of loading steps prescribed to ABAQUS model.

Step	Temperature [C]	Axial Loading [MPa]	Radial Loading [MPa]	Time [s]	Time at Max Amplitude [s]	Electrolyte Phase
Initial	25	0	0	NA	NA	Solid
1	25	1.37	0	10	10	Solid
2	25-352	1.37	0	1	NA	Solid
4	352-500	5.36	15	1	0.5	Molten

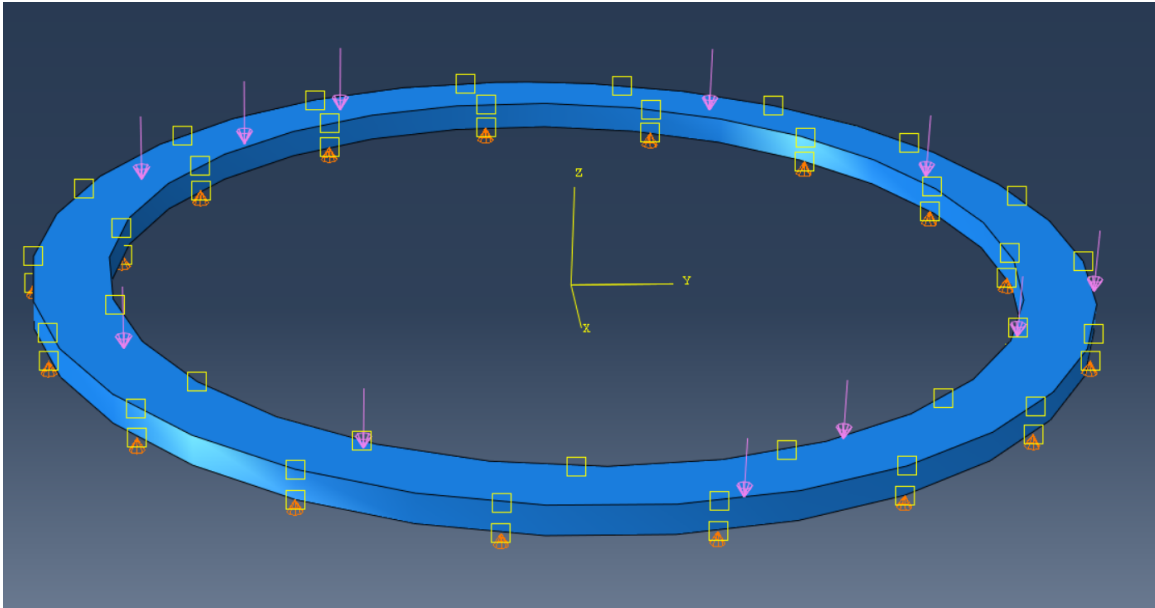


Figure 6. Prescribed axial loading. Electrolyte in solid phase with no radial force exerted.

The axial loading prescribed to the model in Figure 6 initially represents a closing force of 1.37 MPa (200 psi) exerted on a thermal battery stack mentioned in section 2.1. In the separator's solid state, this force would be distributed over the entire area of the ceramic ring and electrolyte pellet. However, once the electrolyte melts it is assumed the load is transferred solely to the ceramic ring. The decreased area of the distributed load results in a pressure of 5.36 MPa. The axial load is then held constant for the remainder of the step.

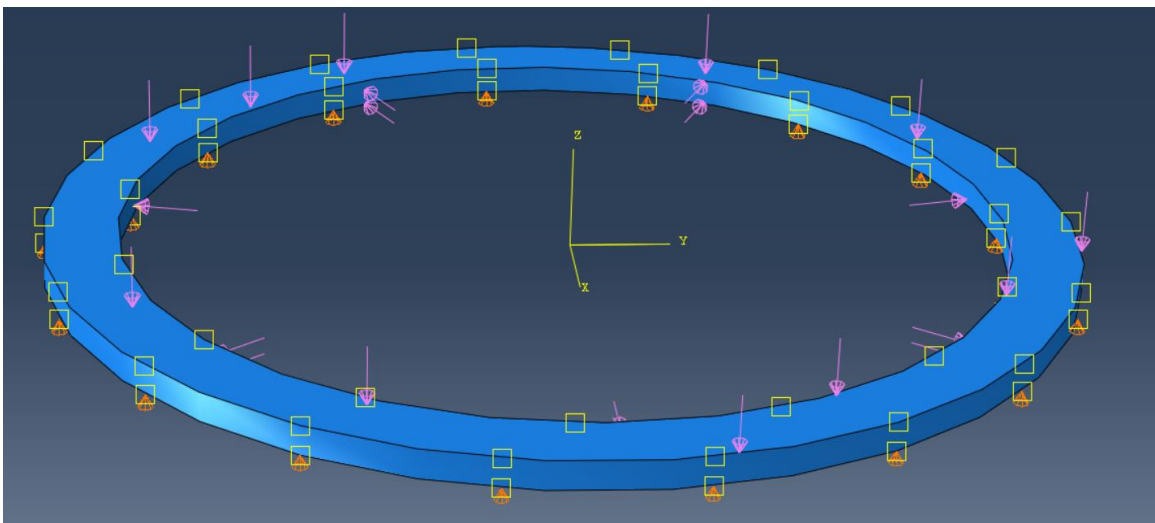
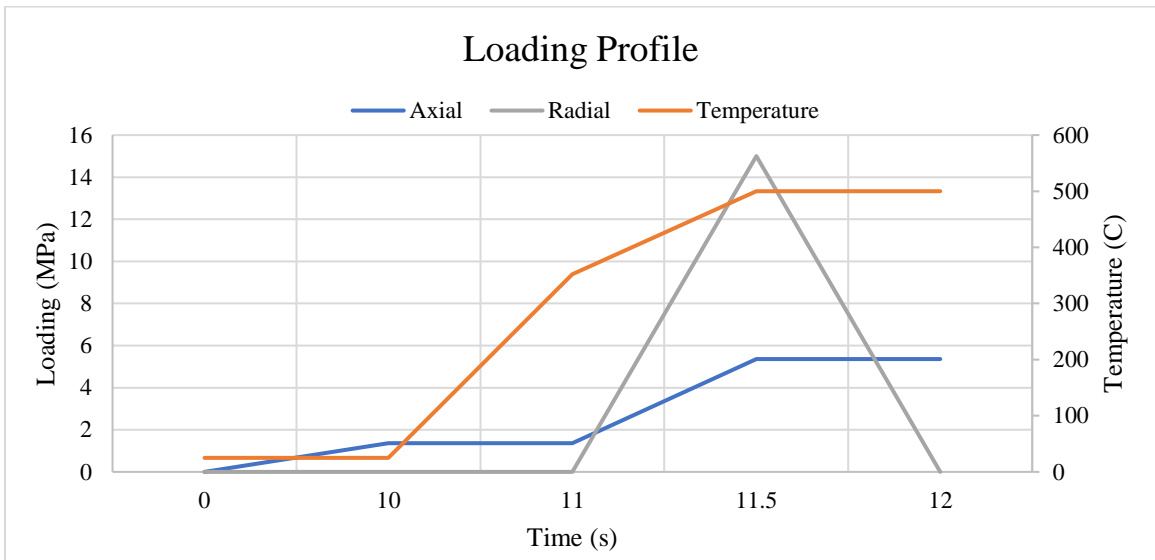


Figure 7. Prescribed axial, radial, and thermal loading of ABAQUS model.

The inner radial load experienced by the MACOR<sup>®</sup> separator ring in step 4 is a result of the LiCl-KCl salt mixtures volumetric expansion from a solid to liquid phase. This is due to the molten salt mixture having a 20-25% lower density<sup>2</sup>. However, to accurately capture the loading experienced by the separator ring, more information would be needed on poromechanical interaction between the electrolyte and electrode pore space. With limited information on this interaction, a pressure was prescribed by assuming the molten electrolyte behaves as an incompressible liquid and transfers the axial force to the inner radial wall as shown in Figure 7. The force linearly ramps to a 15 MPa magnitude in 0.5 seconds of step 4, and proceeds to decay in 0.5 seconds to 0.

Table 2. Mechanical and thermal loading of ABAQUS simulation.



## 2.5 Mesh and Material Properties

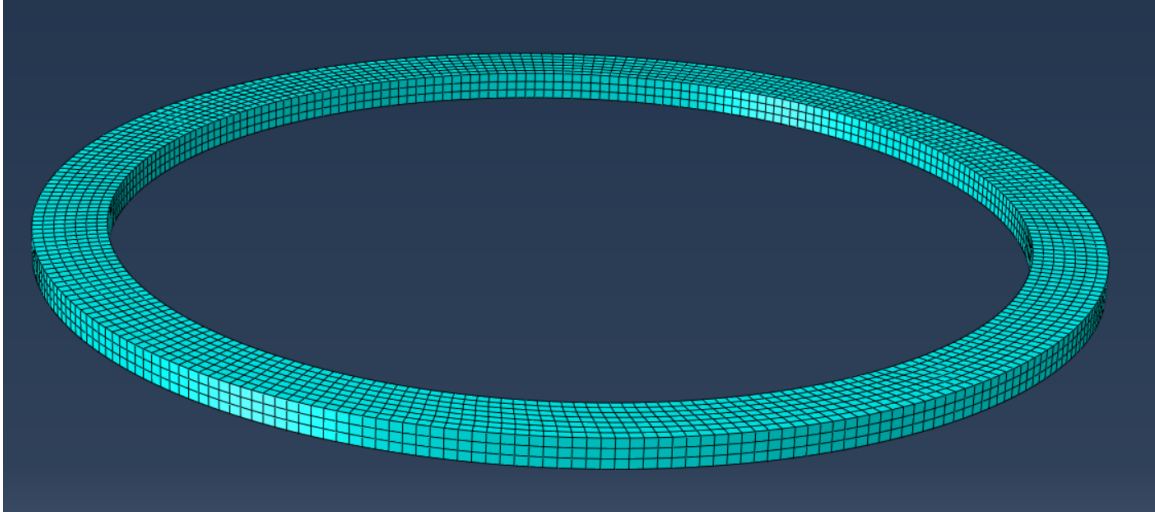


Figure 8. Generated mesh used for ABAQUS model.

For the cylindrical geometry of the part, mesh control options were assigned to a sweep technique and medial axis algorithm. Linear hexahedral 3D stress elements were used to generate the mesh for the ABAQUS model. Axisymmetric approaches to the model could have been used to simplify and potentially cut computation time of the finite element analysis. However, initial attempts of modeling the full part proved to be efficient in run time. A total of 5,838 elements were used with 8896 nodes. The resulting mesh provided adequate resolution and almost no distortions.

Elastic mechanical properties such as Young's modulus, Poisson's ratio, and coefficient of thermal expansion were used to define the MACOR<sup>®</sup> material in ABAQUS. A temperature dependent coefficient of thermal expansion and modulus of elasticity were interpolated from the MACOR<sup>®</sup> ceramic material data sheet in Figures 8-10. Failure criteria and plasticity behavior was not incorporated into the model as it is seen that the modulus of rupture is constant within the prescribed temperature range. However, the results were inspected for values exceeding the specified modulus of rupture.

The modulus of rupture value is used as failure criteria due to the brittle nature of ceramic. Also referred to as flexural strength, the modulus of rupture is typically used in place of a tensile test as failure of ceramics occurs around 0.1% strain. The modulus of rupture typically exhibits the highest stress before a ceramic will yield. Tensile tests are difficult to accurately perform as alignment and sample holding have significant influence on results<sup>14,15</sup>. However, flexural strength obtained from a 3 point bending test is a suitable substitute for ceramics as failure in bending occurs in the extreme outer most fibers in tension of the bottom surface.

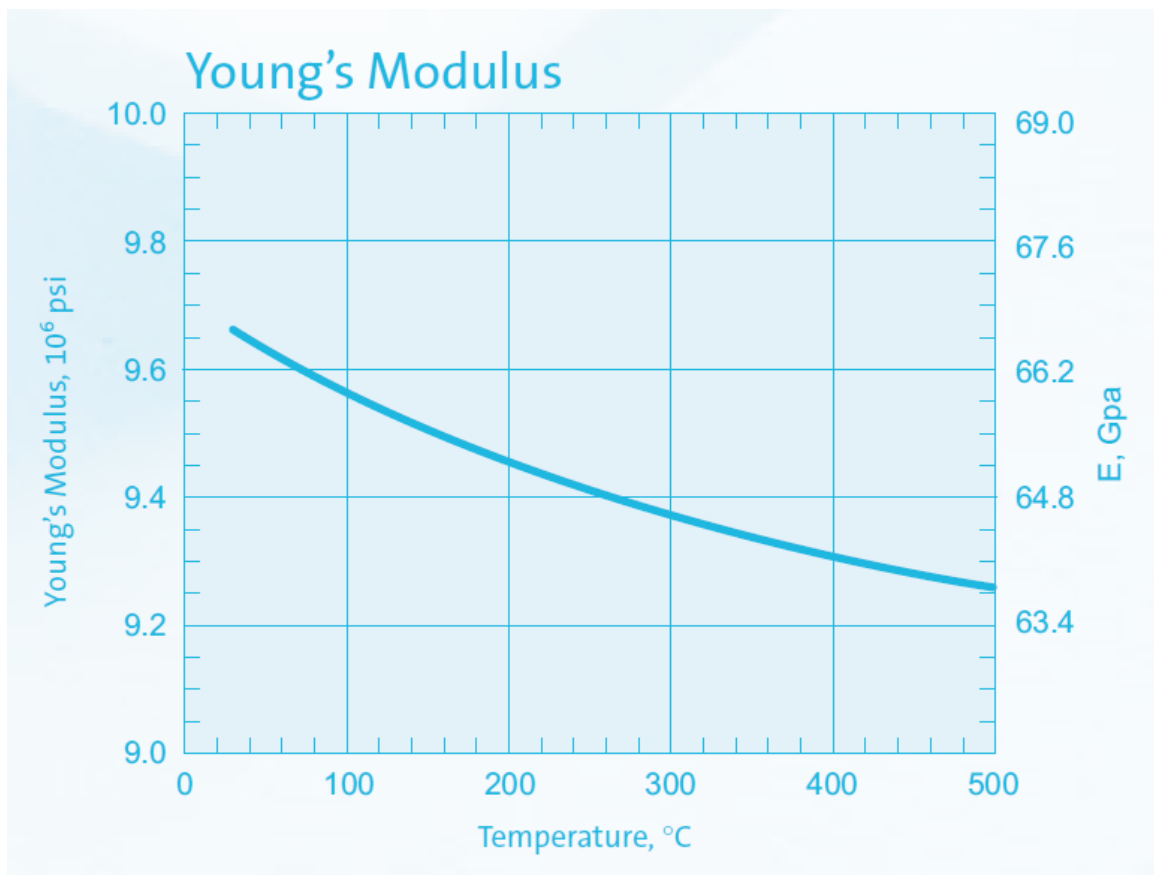


Figure 9. Young's Modulus vs temperature<sup>16</sup>

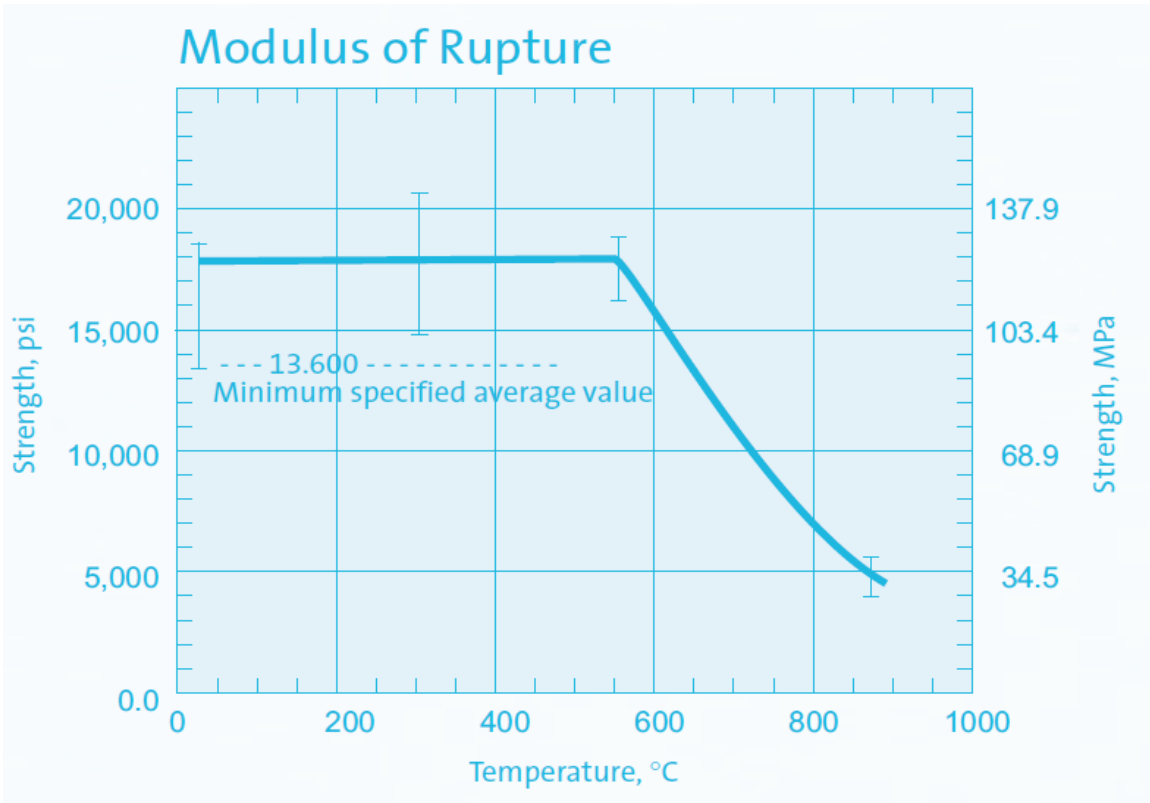


Figure 10. Modulus of rupture vs temperature<sup>16</sup>

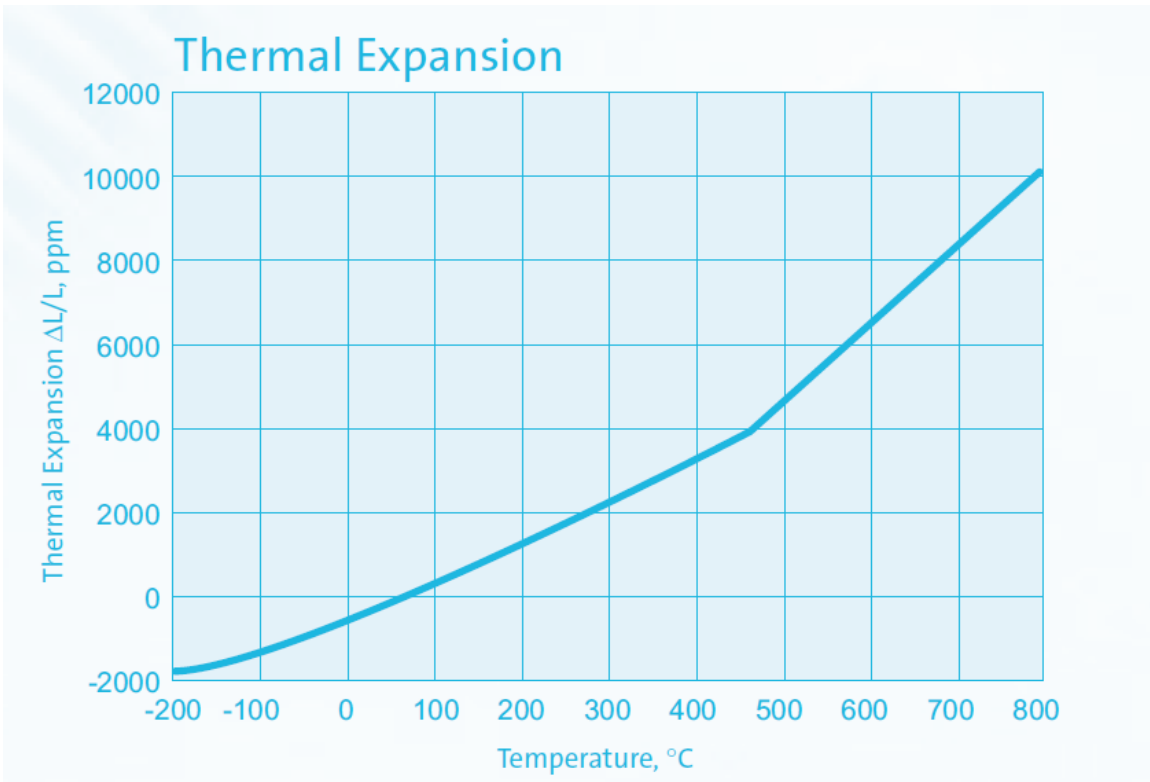


Figure 10. Thermal expansion vs temperature<sup>16</sup>

## 2.6 Mechanical Stability

The ABAQUS software implements model behavior based on user specified material data. Density, Modulus of Elasticity, Poisson's ratio, and a coefficient of thermal expansion (CTE) (Table 4) are used as elastic material properties. Yielding and failure criteria were not incorporate, thus a time independent linear elastic model with heating is described<sup>17</sup>. Stress and strain tensors were generated for the mechanical and thermal loading conditions mentioned in the previous section 2.4. The resulting stresses were then inspected for values exceeding the 94 MPa modulus of rupture (minimum specified average value), or flexural strength from the material data sheet.

## 2.7 Model Theory

An isotropic material is assumed as a directionally independent value for the Young's Modulus, Poisson's ratio, and CTE are provided on the material data sheet. Hooke's law generalized by the first term in EQN 5 describes the linear elastic mechanical strain for an isotropic material. The model undergoes successive uniform temperature increases. The temperature gradient results in a thermal strain shown as the second term in EQN 5. The total strain is expressed in general as EQN 5.

$$\varepsilon_{ij}^{Total} = \varepsilon_{ij}^{el} + \varepsilon_{ij}^T = \frac{1}{E} [\sigma_{ij}(1 + \nu) - \nu\delta_{ij}\sigma_{kk}] + \alpha\delta_{ij}\Delta T \quad (5)$$

$$Where, \quad \delta_{ij} = \begin{cases} for\ i = j, & 1 \\ for\ i \neq j, & 0 \end{cases} \quad (6)$$

The cylindrical geometry of the part makes it convenient to transform the ABAQUS output to a cylindrical coordinate system by EQN's 7 and 8<sup>18</sup>. The directions of interest are the  $rr$  (radial direction),  $\theta\theta$  (Hoop direction), and  $zz$  (axial direction) shown in Figure 11. The transformation results in an axisymmetric stress and strain distribution as shown in Figures 12-13. The resulting tension and compressive behaviors of the part are indicated by positive and negative stress and strain values respectively. It can be seen in Figure 13 that the largest stress and strain values occurs in tension for the  $\theta\theta$  direction.

$$\sigma' = \beta_{ip}\beta_{jq}\sigma_{pq} \quad (7)$$

$$\varepsilon' = \beta_{ip}\beta_{jq}\varepsilon_{pq} \quad (8)$$

$$\text{Where, } \beta_{ij} = \begin{bmatrix} \cos\theta & \sin\theta & 0 \\ -\sin\theta & \cos\theta & 0 \\ 0 & 0 & 1 \end{bmatrix} \quad (9)$$

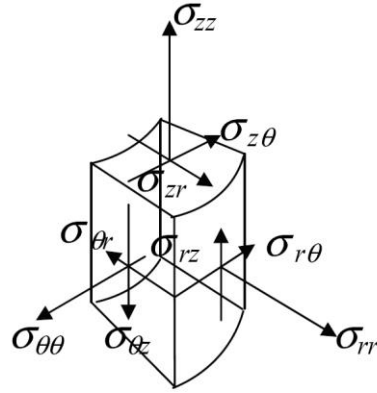


Figure 11. 3D Cylindrical Element<sup>18</sup>

## 2.8 FEA Results

The stress distributions of the  $rr$ ,  $\theta\theta$ , and  $zz$  directions were captured at approximately  $t=0.5$  seconds of step 4. This is when the amplitude of the loadings and resulting stresses are the greatest. The stress distributions were compared to the modulus of rupture and compressive strength values provided by the material data sheet. The 94 MPa minimum specified average value for the modulus of rupture value is reached in the  $\theta\theta$  direction. However, the average value of 123.2 MPa also shown on the material data sheet is not exceeded.

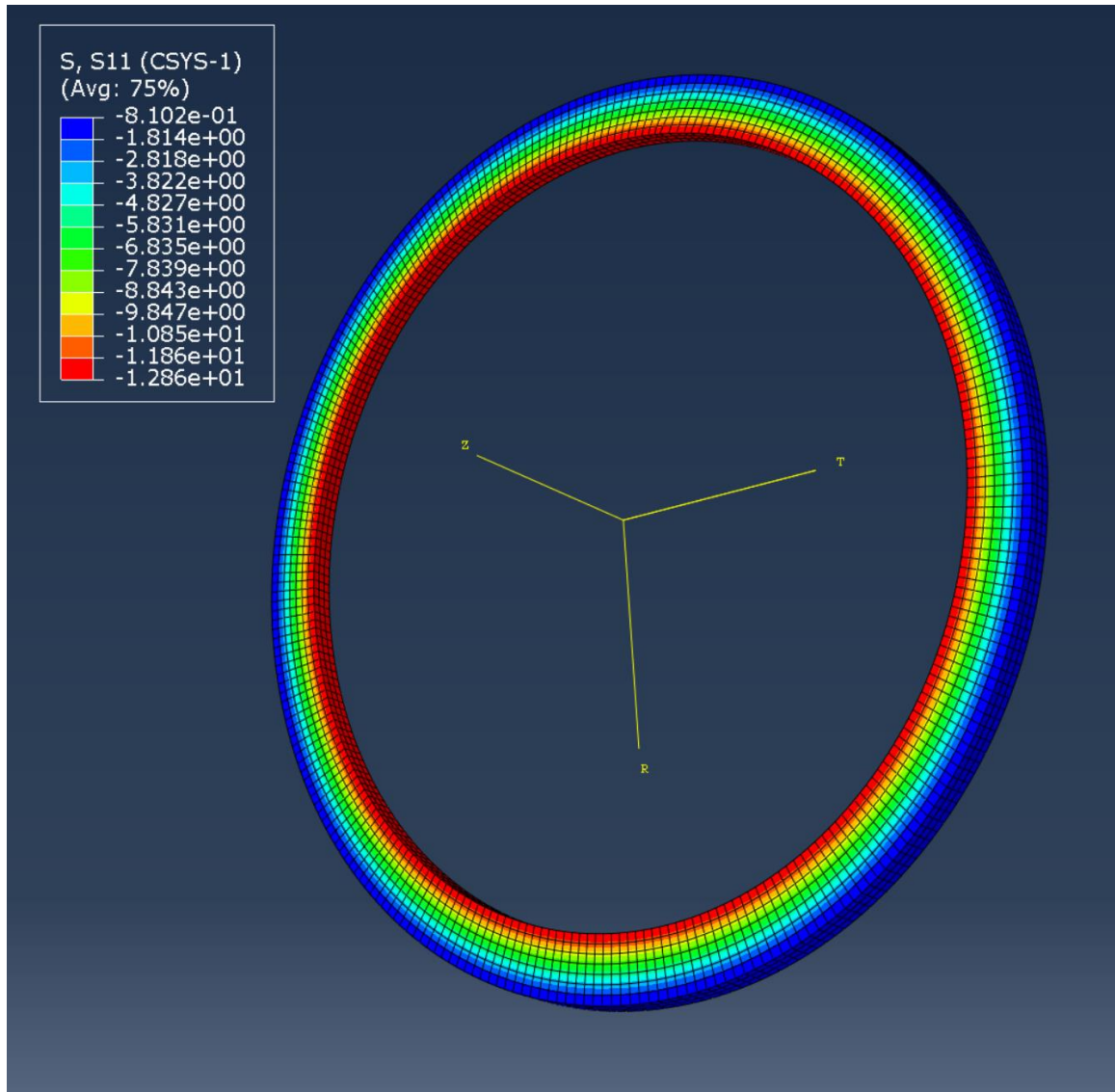


Figure 12. Radial stress distribution (rr direction) at t=0.5 sec of loading step 4.

An axisymmetric stress distribution due to the coordinate transformation occurs for the rr (radial) direction as shown in Figure 12. The negative values for the rr and zz directions indicate the part is in compression. The maximum amplitude of stress occurs at the inner radial wall. The compressive stress is a results of the inner radial pressure prescribed which represents a force exerted by the electrolyts expansion (not shown). The MACOR<sup>®</sup> ceramic has a compressive strength of 345 MPa and would likely fail in tension in the Hoop direction before this is reached.

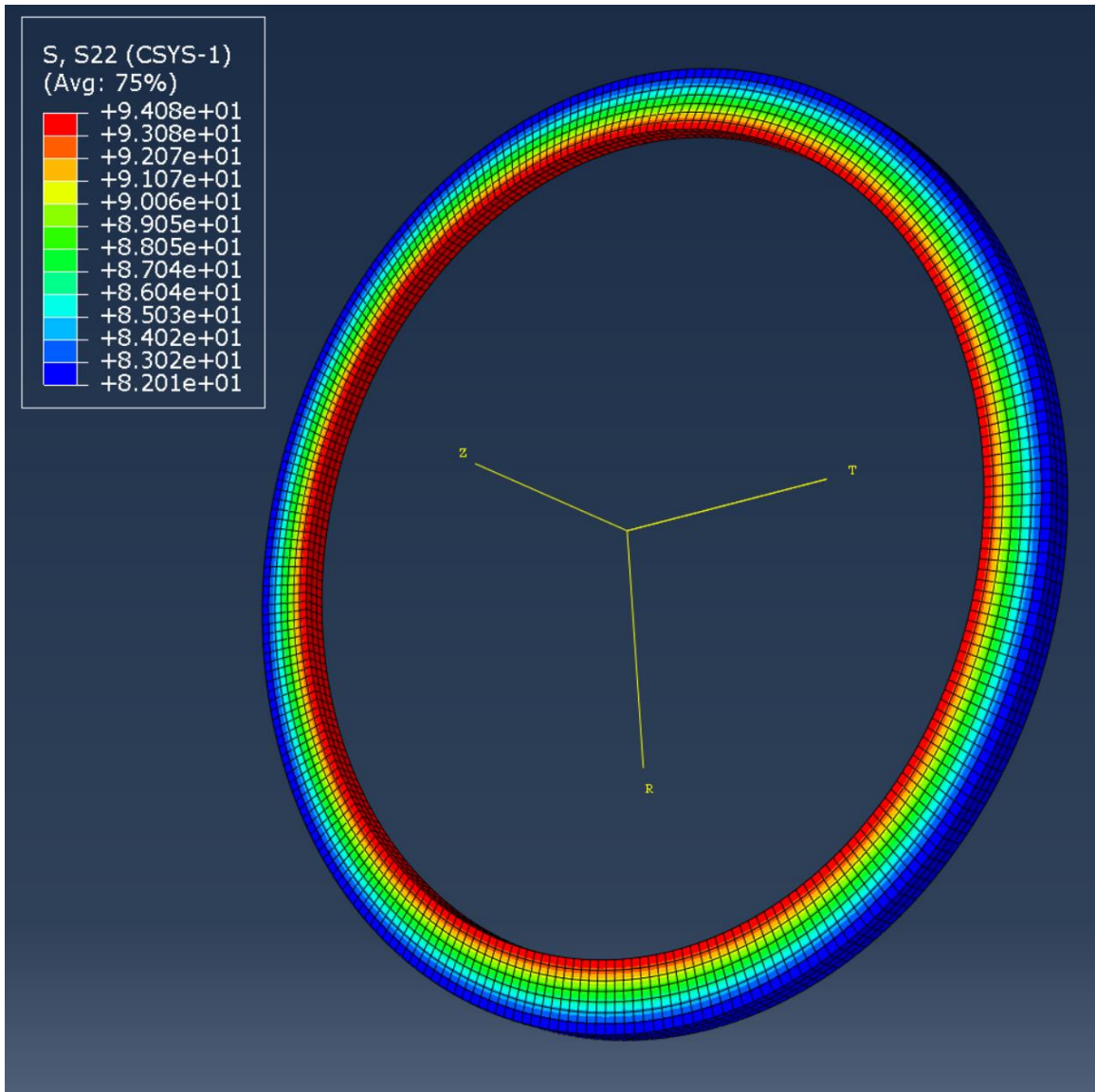


Figure 13. Hoop stress distribution ( $\theta\theta$  directions) at  $t=0.5$  sec of loading step 4.

The  $\theta\theta$  or Hoop direction also results in an axisymmetric stress distribution. There is no contribution from thermal loading for this direction as the part is free to expand. However, the inner radial pressure and Poisson effect put the part in tension as indicated by the positive values. A maximum stress of approximately 94 MPa is reached at the inner radial wall, the same as the minimum specified average value listed on the MACOR<sup>®</sup> material data sheet. It is interpreted that the part is likely reaching its limits and that the resulting load from an expanding electrolyte should be taken into careful consideration.

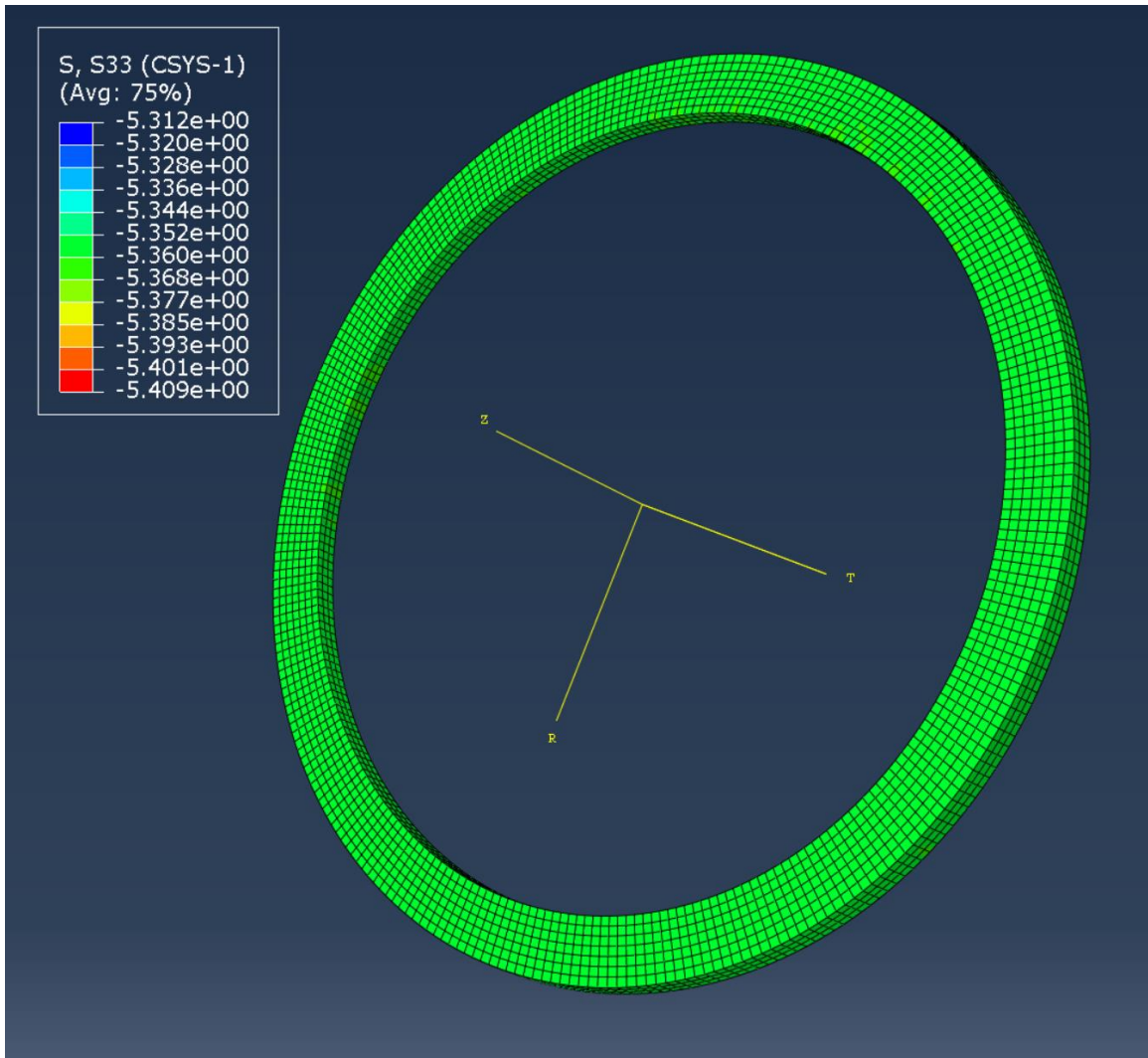


Figure 14. Axial stress distribution (zz direction) at t=0.5 sec of loading step 4.

Figure 14 shows the resulting stress for the zz direction in compression. The max amplitude stays near the prescribed 5.36 MPa axial load for this step. The overall magnitude of stress for all 3 principle directions are show in Figure 15. The Poisson effect can be seen in the strain behavior of Figure 16. However, there are no contacting surfaces to oppose the parts thermal expansion and it is likely that the stresses generated are independent of temperature changes.

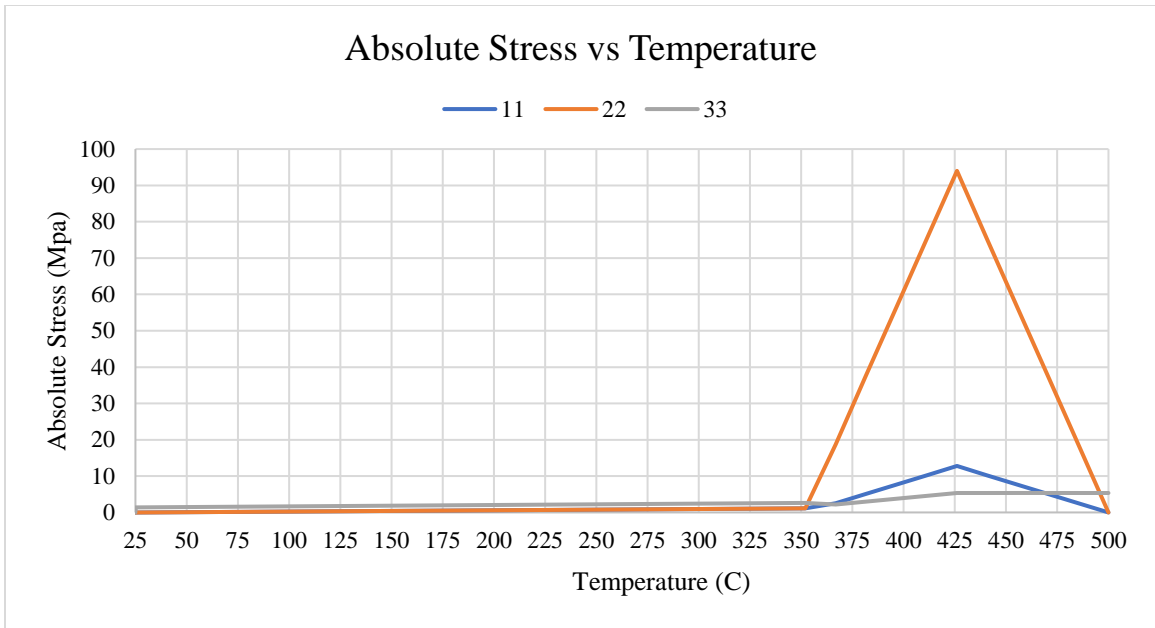


Figure 15. Absolute stress vs temperature

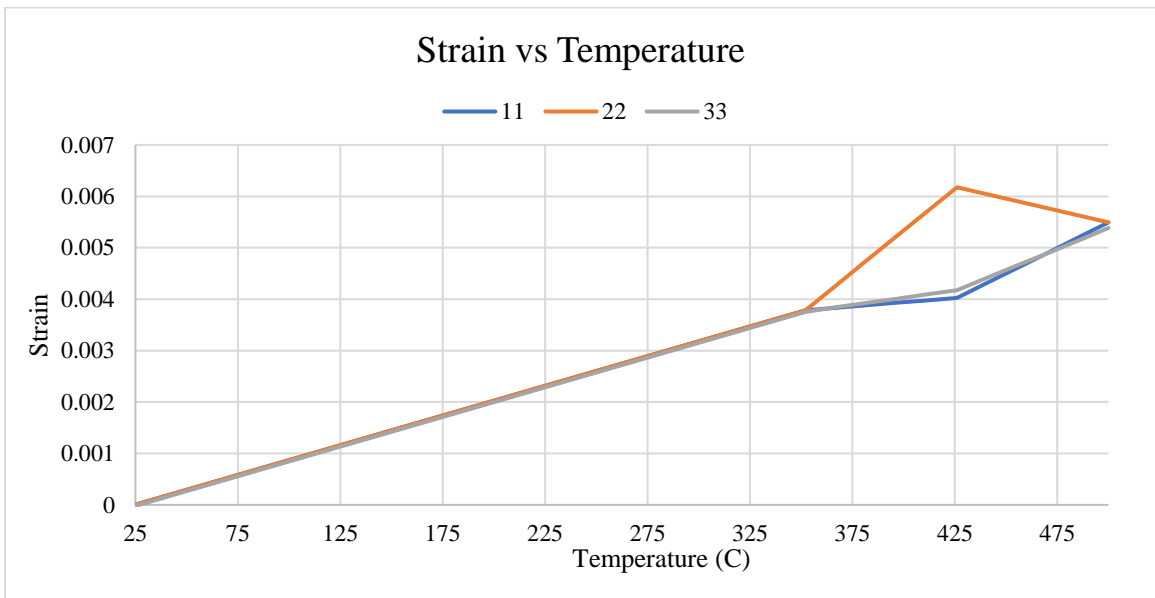


Figure 16. Strain vs temperature

## 2.9 Validation

To ensure the ABAQUS model captures both the linear elastic behavior and heating effects, the elastic and thermal strain outputs were used to verify the generated stress. Inverting the first term of EQN 5 leads to the elastic stress as shown by EQN 10. The simulation stress values were obtained using only the elastic strain output. This indicates that the general static analysis stresses generated in the part are not influenced by the temperature change. A more detailed model is needed to capture heating effects and interactions with other components such as the electrodes and electrolyte.

$$\sigma_{ij} = \frac{1}{(1 + \nu)} \left[ \varepsilon_{ij} + \frac{\nu}{(1 - 2\nu)} \delta_{ij} \varepsilon_{kk} \right] \quad (10)$$

## Chapter 3 Electrochemical Characterization

### 3.1 Material Preparation and Electrochemical Procedures

Two types of cells were built to compare the electrochemical performance of the experimental separator design to that of a traditional pellet. “Single cells” which contain an anode, cathode, and separator were built for discharge testing, while cells with only a separator were built for electrical impedance spectroscopy (EIS). A control and experimental variation were made for each type of cell. The control cells utilized a 65/35 wt% LiCl-KCl/MgO separator pellet, while the experimental contains an all LiCl-KCl pellet in combination a MACOR<sup>®</sup> ceramic ring (Figure 17). Both the control and experimental single cells were built with a FeS<sub>2</sub> cathode, separator (both control and experimental), and LiB anode by stacking them in series.

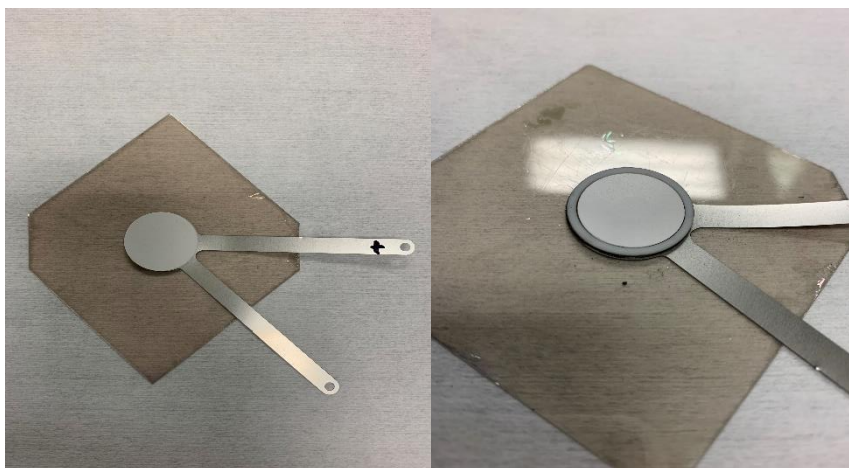


Figure 17. Single cell being assembled with control pellet separator (left) and experimental separator (right).

The anode was made from a 70/30 Li/B alloy foil. This foil was punched to a 0.750” diameter using a Di-acro punch and die. The FeS<sub>2</sub> cathode and control separator pellets (65/35 LiCl-KCl/MgO) were made using a 20-ton mechanical press and die with an outer diameter of 0.7562”. An 8-ton pressing force, 9 second dwell-time, and 7-ton stripping force were used to achieve the target thickness. These pellets were pressed to 0.020”  $\pm$  0.001 for handling purposes.

Table 5. Details for anode, cathode, and control separator.

Material	Mass [g]	Theoretical Density [ $\frac{g}{cm^3}$ ]	Density [ $\frac{g}{cm^3}$ ]	Volume [ $cm^3$ ]
Anode	0.0225 $\pm .001$		$0.789 \pm .0005$	$0.028 \pm .0005$
Cathode	$0.40 \pm .01$	4.36	$2.71 \pm .01$	$0.00898 \pm .00039$
Separator	$0.30 \pm .01$	2.56	$2.03 \pm .01$	$0.00898 \pm .00039$

The experimental separators were built using a LiCl-KCl pellet in combination with the MACOR<sup>®</sup> ceramic ring. This ring was machined from bulk to a thickness of  $0.020 \pm .001$ . Two separate versions of the parts were designated “SR10” and “SR35”, corresponding to 10 and 35 mass percentages of the separator respectively as mentioned in section 2.1. The LiCl-KCl salt pellets were pressed using the same process for the cathode pellet. The geometry of salt pellet and MACOR<sup>®</sup> ceramic ring are listed in Table 6. It should be noted that most of the final geometries used were driven by available tooling.

Table 6. Experimental separator details of LiCl-KCl pellet and MACOR<sup>®</sup> ceramic ring.

Part	OD [in]	ID [in]	LiCl-KCl Pellet OD [in]
SR10	$0.7562 \pm .005$	$0.7279 \pm .002$	0.718
SR35	$0.7562 \pm .005$	$0.6519 \pm .002$	0.6430

### 3.2 Single Cell Testing and Electrical Impedance Testing

Both single cell and electrical impedance testing were performed on a custom test fixture (Figure 18) with a heat source, 6.42 lb axial load, and voltage/current lead connections. Single cell discharge data was recorded using a Maccor model 4200 automated tester. Electrical impedance data was gathered using a Solartron Frequency Response Analyzer (FRA). The frequency response was run at an open circuit potential of 10 mV over a range 0.1-10<sup>5</sup> Hz. Post processing of the collected data was performed in ZView and Microsoft Excel.

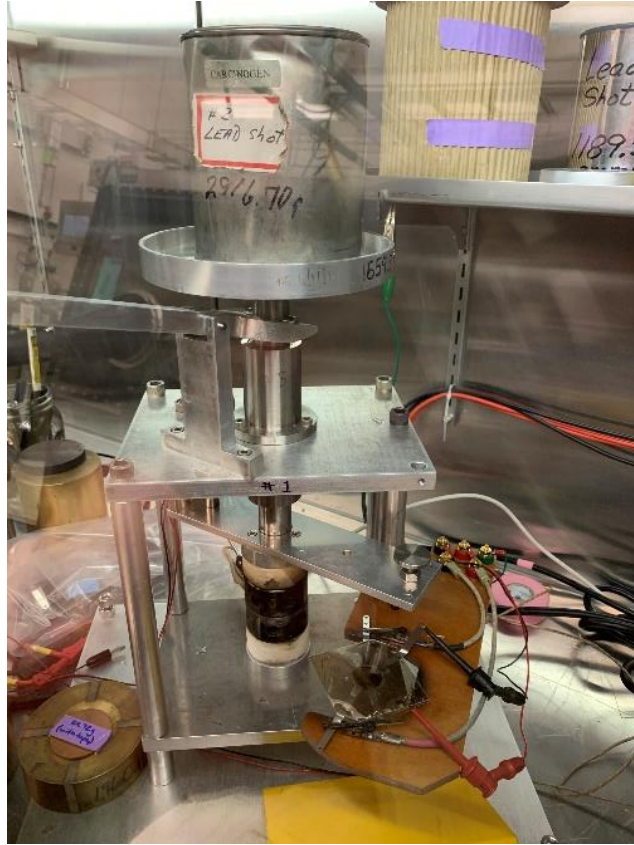


Figure 18. Single cell test fixture.

### 3.3 Electrochemical Performance

As discussed previously in the introduction, traditional separator design inherently results in a trade-off between mechanical stability and electrochemical performance. Here we examine how the experimental separator design compares to that of a traditional pellet by means of EIS and discharge testing. Analysis of EIS data will allow us to compute a metric of conductivity to which we can compare the separators electrochemical performance as individual components. We will also gain insight as to how the separators function as part of an assembled single cell via current pulse discharge test that allows us to examine pulse resistivity and compute a total delivered cell capacity. These parameters are crucial metrics of thermal batteries and ultimately the feasibility of the experimental separator design.

### 3.4 Conductivity

Conductivity, or the reciprocal of resistivity show in EQN 11 is of most importance when comparing traditional separator pellets to the experimental design that utilizes a MACOR<sup>®</sup> ceramic ring. In our control and experimental separators, we are concerned with ionic conductivity which is a mechanism of our systems ability to pass current<sup>2</sup> by means of the ionic species migration. The cell constant  $\left(\frac{t}{A}\right)$  is a geometrical correction to the active area A shown in Figure 19. In the case of our control cells, A is the entire cell area and for the experimental cells it is the inner diameter of the ceramic. The value of R is derived from our EIS data and AC impedance analysis.

$$k = \frac{1}{R} \left( \frac{t}{A} \right) \quad (11)$$

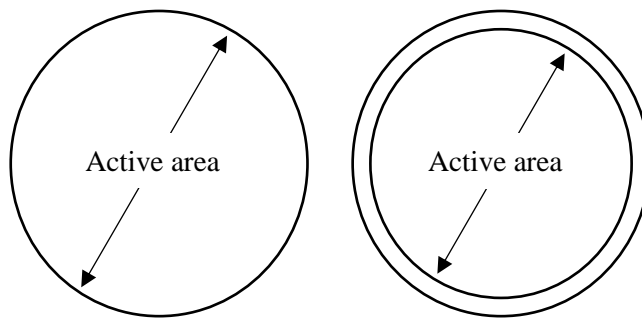


Figure 19. Active area (A) for traditional pellet (left) and experimental (right) separator

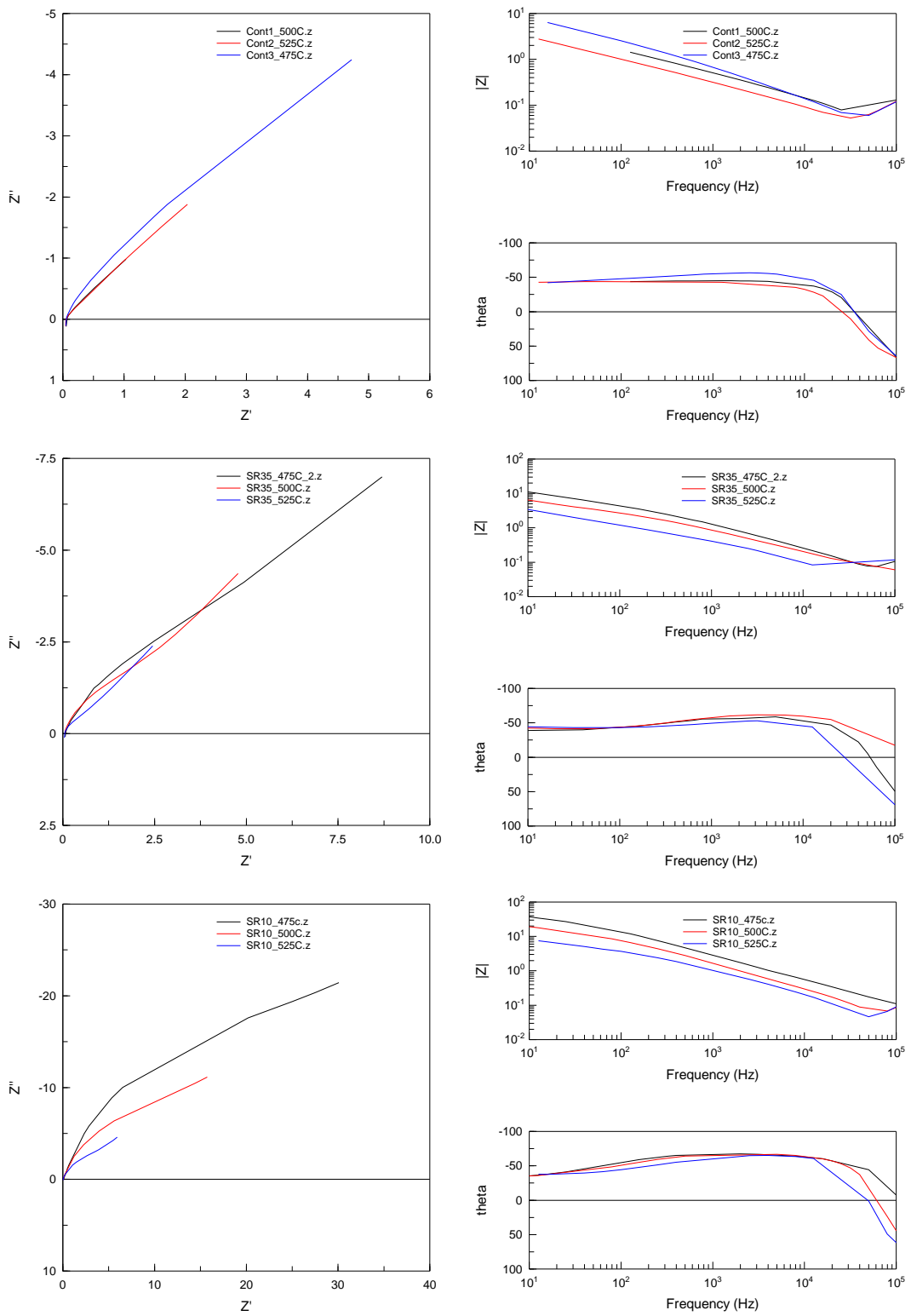


Figure 20. Frequency response data for control and experimental separators at 475C, 500C, and 525C.

The derivation of R used to find our separator conductivities starts by elaborating on the resistivity of an electrochemical system. Using AC circuit theory, it is possible to distinguish which mechanisms contribute to potential drops across a separator by analysis of their frequency response<sup>18</sup>. Ohm's law (EQN 12) a useful tool in circuit analysis can be expressed in terms of a radial frequency and phase angle (EQN 13). Equivalent circuits have been studied and found to correlate with specific electrochemical processes to which it is also useful to express impedance in terms of real and imaginary components (EQN 14). Combinations of circuit elements that capture the behavior of a separator's AC frequency response are chosen to characterize the system, and ultimately find a value of R used in conductivity calculations.

$$R = \frac{V}{I} \quad (12)$$

$$Z = Z_0 \frac{\sin(\omega t)}{\sin(\omega t + \phi)} \quad (13)$$

$$Z(\omega) = Z_0(\cos(\phi) + j\sin(\phi)) \quad (14)$$

Figure 20 shows EIS data for the control and experimental separators swept over a frequency range of 10-10<sup>5</sup> Hz at 10mV. It's immediately evident that the magnitude of impedance for the experimental cells is greater than the control. A more prominent semi-circular region also develops in the experimental cell Nyquist plots. The expression for the linear region (EQN 15) is derived from an equivalent circuit of a resistance and capacitor in series and is known as the Warburg impedance<sup>19</sup>. This region is an attribute of diffusion limitations. The semi-circular region results from a rate limited charge transfer process and is expressed as (EQN 16)<sup>20</sup>.

$$Z_W = R_W + \frac{1}{i\omega C_W} \quad (15)$$

$$Z_{CT} = \frac{R_{CT} + i\omega R_{CT}^2 C_D}{1 + \omega R_{CT}^2 C_D^2} \quad (16)$$

The equivalent circuit in Figure 21 was built to model the control cells and results in an exceptional fit for all 3 temperatures. There are no electrodes in the system and thus no mechanisms of charge transfer. The (R1) resistor is the systems electrolyte resistivity and the constant phase element (CPE1) in parallel with a Warburg element (Wo1) represents a double layer capacitance and diffusion respectively. The constant phase element was used in place of a traditional capacitor due to a nonhomogeneous electrolyte contact<sup>21</sup> between the MgO/LiCl-KCl mixture and stainless-steel current collector. Some inductance is also observed in the system and compensated for by the (L1) element.

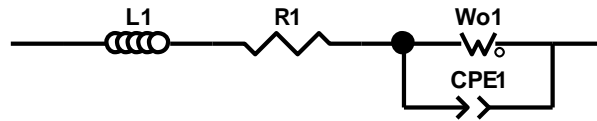


Figure 21. Equivalent circuit for traditional MgO/LiCl-KCl pellet system.

When modeling the equivalent circuit in Figure 22 to fit the experimental cells EIS data, a circuit consistent with a charge transfer process emerged. As mentioned previously, having no electrodes in the system would suggest a charge transfer process occurring between the LiCl-KCl and MACOR<sup>®</sup> ceramic. The introduction of LiCl to the bulk constituents (SiO<sub>2</sub>, B<sub>3</sub>O<sub>2</sub>, AlO<sub>2</sub>) of the ceramic at elevated temperatures may start to form ionically conductive glasses as mentioned in Meikhail et al<sup>21</sup>. The magnitude of impedance is seen to increase with the inner radial area of the MACOR<sup>®</sup> ceramic ring. However, the extent of reactivity, geometric influence, and leakage impedance mechanism is not distinguishable.

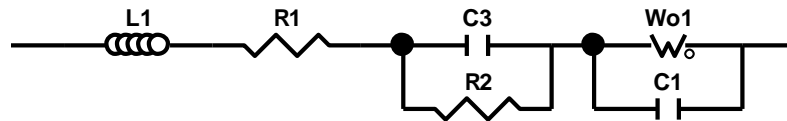


Figure 22. Equivalent circuit for experimental separator system.

To quantify the goodness of fit for the equivalent circuit models, chi-squared, sum of square, and individual element error values are generated from the Z view software (Appendix A). The control cell chi-squared and element error values increase with temperature but remain exceptionally small. The SR35 experimental cells yield chi-squared and element error values of increasing magnitude. By visual inspection of the fit lines for the SR35 500C, SR10 475C, 500C, and 525C, it is evident that the equivalent circuit does not fully capture the data. The deviation may be linked to a physical problem such as electrolyte leakage, reactivity with the MACOR<sup>®</sup> ceramic ring, or geometric influences with an increase in surface area.

The total impedance of the experimental separators can be expressed in EQN 17 by applying standard methods to the equivalent circuit in Figure 22. As we take the limit of the frequency  $\omega \rightarrow \infty$ , it is assumed that the Warburg impedance is very small compared to that of the charge transfer and EQN 19 (expressed in its real and imaginary components). The limit yields a value of the electrolyte resistance  $R_E$ . A similar value results for the control cells as there is only a Warburg element in parallel with a constant phase element and electrolyte resistance. Interpreting this limit from the EIS data, the real component of Z was taken at the highest frequency and used for the R value of our conductivity calculations.

$$Z_{TOTAL} = \sum_{i=1}^n Z_i, \quad \text{Where } i \text{ denotes the impedance type} \quad (17)$$

$$Z_{TOTAL} = R_W + \frac{1}{i\omega(C_{DC} + C_W)} + R_E + \frac{R_{CT}}{1 + \omega R_{CT}^2 C_D^2} + \frac{i\omega R_{CT}^2 C_D}{1 + \omega R_{CT}^2 C_D^2} \quad (18)$$

$$\lim_{\omega \rightarrow \infty} R_W + \frac{1}{i\omega(C_{DC} + C_W)} + R_E + \frac{R_{CT}}{1 + \omega R_{CT}^2 C_D^2} + \frac{i\omega R_{CT}^2 C_D}{1 + \omega R_{CT}^2 C_D^2} \quad (19)$$

$$\lim_{\omega \rightarrow \infty} Z_{CT} \Rightarrow Z_W \cong 0 \quad (20)$$

$$\lim_{\omega \rightarrow \infty} R_W + \frac{1}{i\omega(C_{DC} + C_W)} + R_E + \frac{R_{CT} + i\omega R_{CT}^2 C_D}{1 + \omega R_{CT}^2 C_D^2} \quad (21)$$

$$= R_E$$

Figures 23 and 24 show the compiled specific conductivities for the control and experimental separators that have been normalized by the cells active area. It can be seen that the control cell conductivities were hardly responsive to an increase in temperature while the experimental separators were highly responsive. Figure 25 also shows the geometric dependence of conductivity as it is seen to decrease with increasing active area. The geometric and temperature dependence of conductivity offer tunable parameters for the experimental separator cells. However, further characterization of reactivity or investigation of an alternative ceramic material may yield more desirable results.

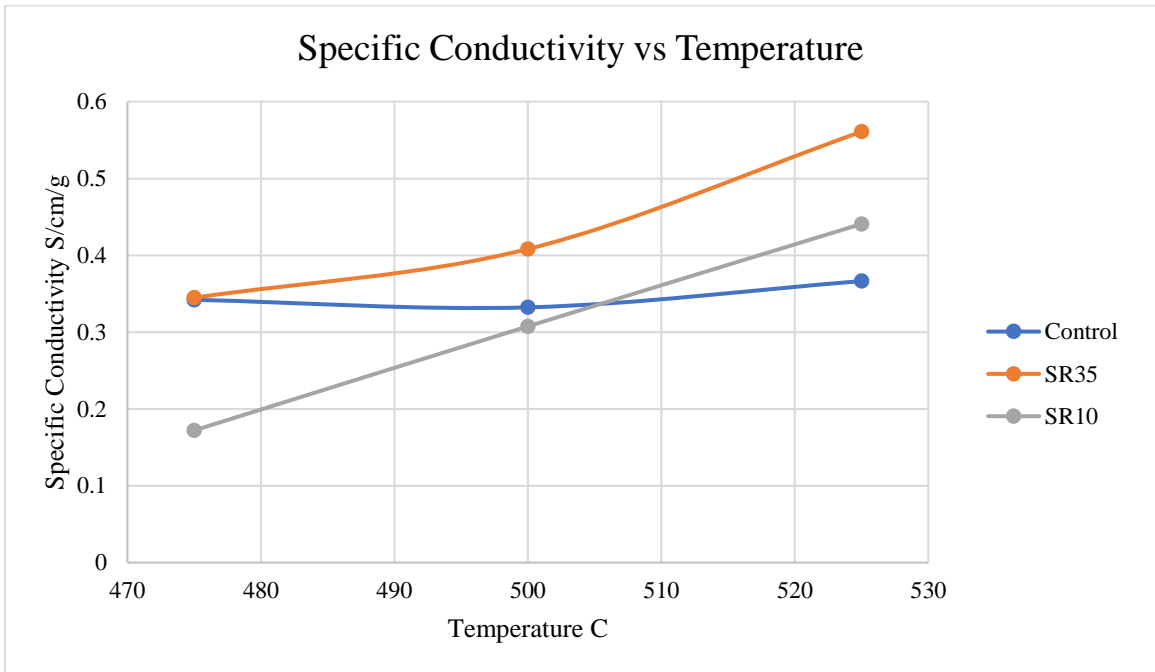


Figure 23. Specific conductivity of experimental separator cells.

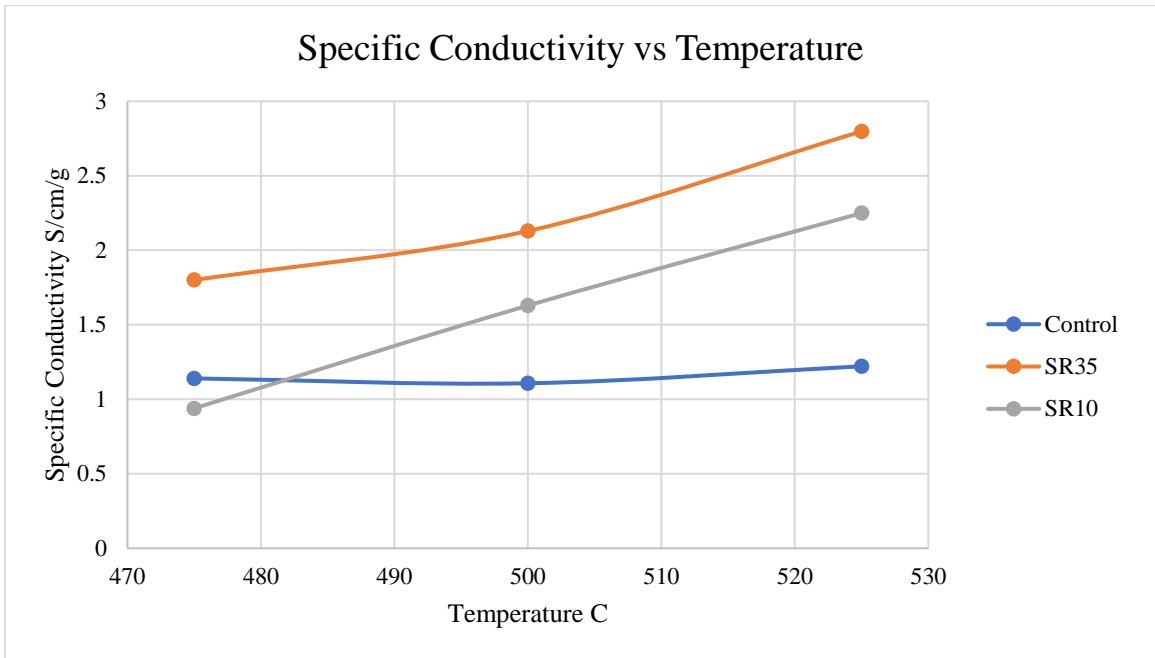


Figure 24. Specific conductivity normalized by active area and mass.

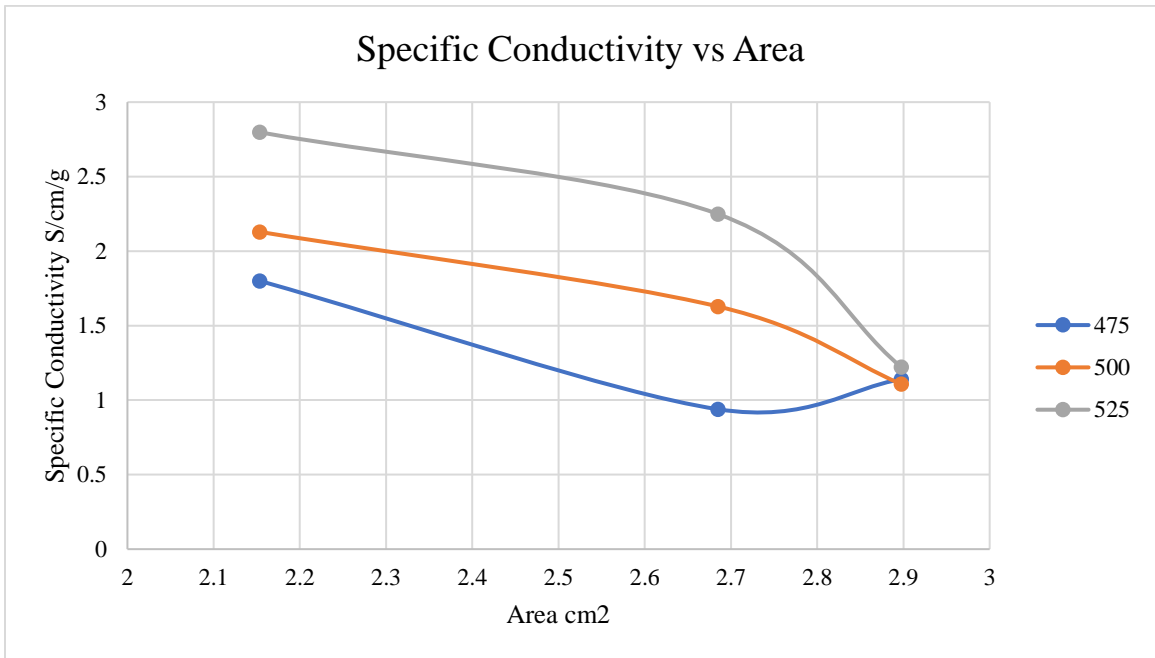


Figure 25. Specific conductivity (normalized by active area and mass) vs active area.

### 3.5 Current-Pulse Discharge Performance

To understand how the experimental separator performs as part of a single cell battery system, a discharge profile was created for a desired current density of  $2 \left[ \frac{A}{cm^2} \right]$ . For the given discharge profile, a required capacity (EQN 19) was determined for the single cell's anode and cathode using their respective active materials. The LiB anode and FeS<sub>2</sub> cathodes specific capacities  $\left[ \frac{mAh}{g} \right]$  were used to ensure the electrodes had a sufficient capacity to complete the discharge profile (Table 4). The mass for the cathode and separator pellets were ultimately chosen based on pellet robustness.

$$q = \int_{t_0}^t I dt \quad (22)$$

Table 3. Anode and cathode capacity details.

Material	Specific Capacity $\left[ \frac{mAh}{g} \right]$	Required Capacity [mAh].	Actual Mass [g]	Actual Capacity [mAh].
Anode	1333.3 <sup>24</sup>	6.96	0.0225	30
Catholyte (73.5% Active Material)	335.0 <sup>13</sup>		0.40	98.4

Figure 25 shows the current-pulse voltage response for both control and experimental single cells at 475, 500, and 525C. It can be seen for the control cells that the voltage drops during the applied load are significant but decrease in magnitude the elevated temperature. Figure 26 shows the entire discharge curves at 500C, where two distinct plateaus appear for the control and correspond to the discharge process of available Li within the LiB foil. The first plateau is the discharge of metallic lithium within the matrix and then the secondary plateau corresponds to the reduction of the Li in the LIB matrix

itself<sup>22</sup>. The delivered capacities in Figure 28 indicate the experimental cells deliver far less than the control.

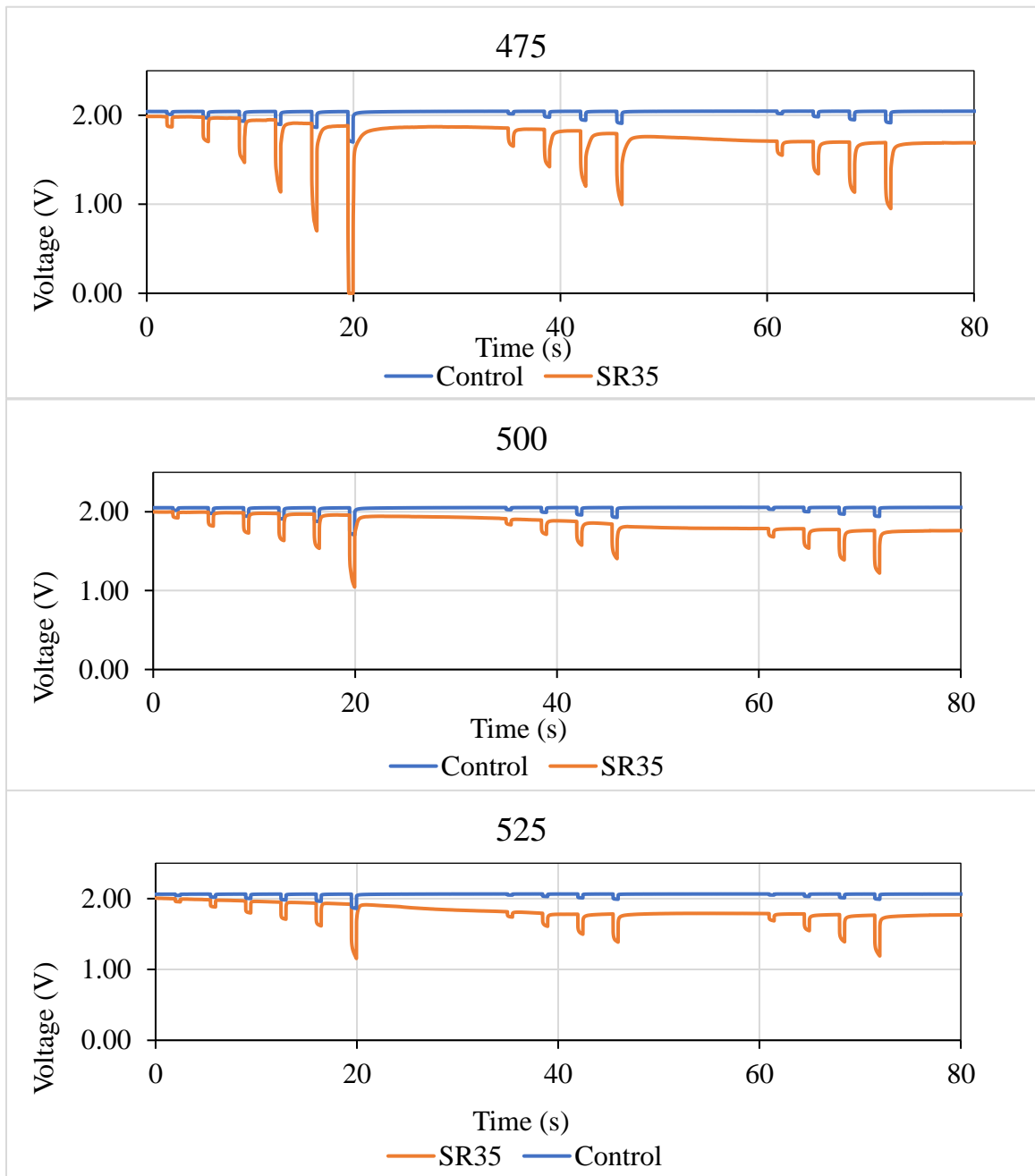


Figure 26. Current-pulse voltage responses for the control and experimental (SR10, SR35) single cells at 475, 500, 525C.

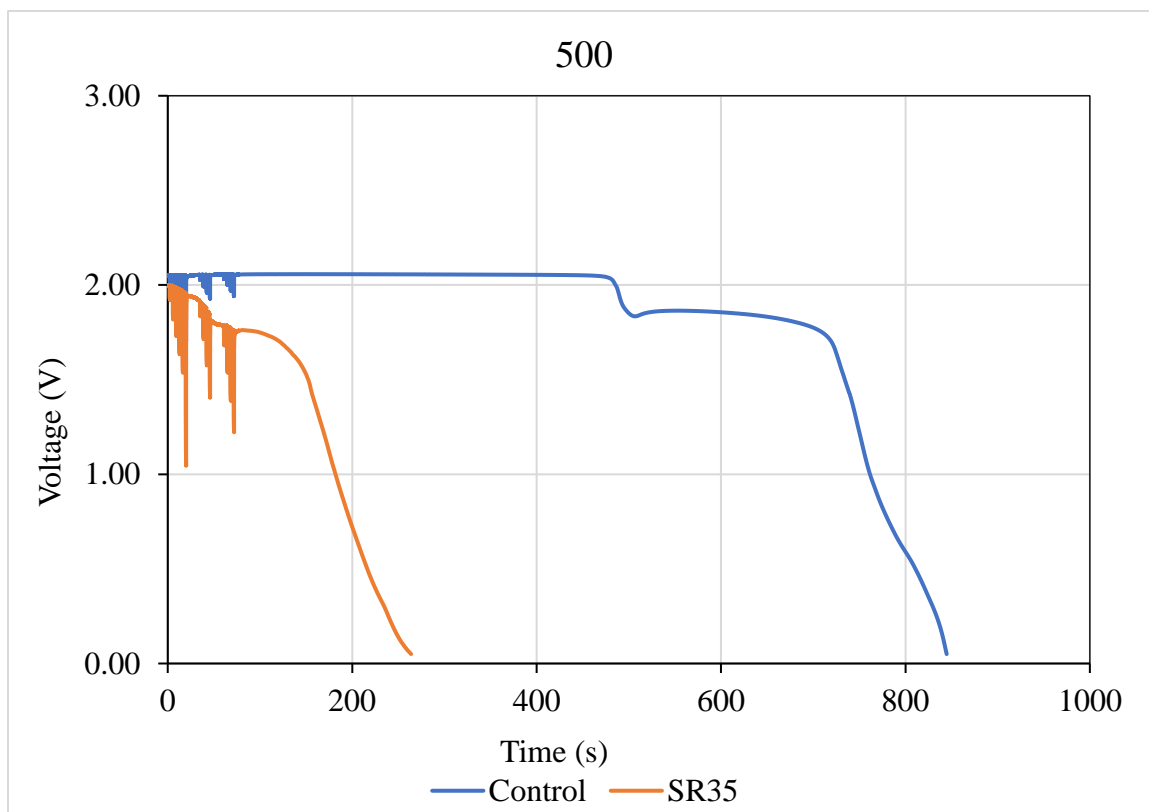


Figure 27. Typical discharge curve of experimental separator single cell with LiB anode and FeS<sub>2</sub> cathode.

The shape of the experimental separator discharge curve is significantly different than the control. Possible contributions to this variation include anode reactivity with SiO<sub>2</sub> (the bulk constituent of the MACOR<sup>®</sup> ceramic), electrolyte leakage, and accelerated consumption of lithium. During single cell testing, it was observed that electrolyte was consistently able to escape from the cells at the ceramic ring-electrode interface, possibly causing the cell to have desultory active areas. Additionally, the direct contact of electrolyte to the electrode is likely to have accelerated the consumption of Li, thus depleting the anode capacity rapidly. The extent of these contributions to the overall diminished performance of the single cell merits further investigation.

Figure 27 shows the current pulse resistivities for both control and experimental single cells at 475, 500, and 525C. The controls cells remain relatively constant while the experimental cells suffer a greater pulse resistivity with the subsequent number of pulses and decrease in temperature. The pulse resistivity is an important metric of a thermal battery as it characterizes the voltage drop due to an applied load. As seen in Figure 25 a more significant voltage drop also consequently results in a time delay or “shoulder” for the voltage recovery. The pulse resistivity (EQN 20) takes these voltage recoveries into account by averaging the resting voltage and current before and after the voltage drop.

$$R_p = \frac{\Delta V}{\Delta I} = \frac{avg(V_{rest}) - V_{Pulse}}{avg(I_{rest}) - I_{Pulse}} \quad (20)$$

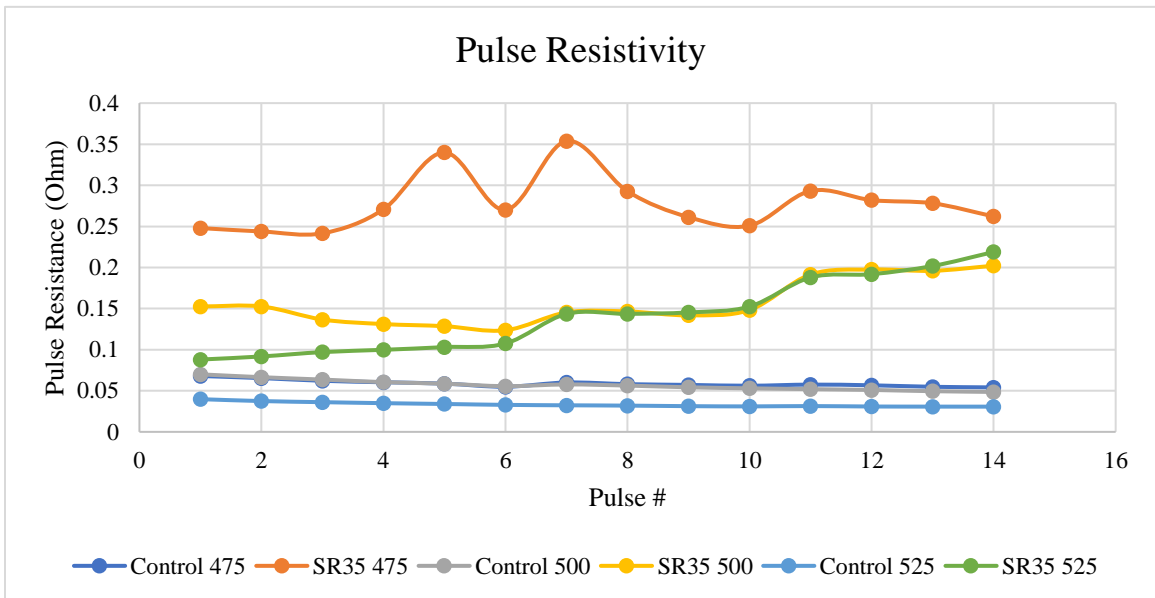


Figure 28. Compiled pulse resistivities for control and experimental cells at 475, 500, and 525C.

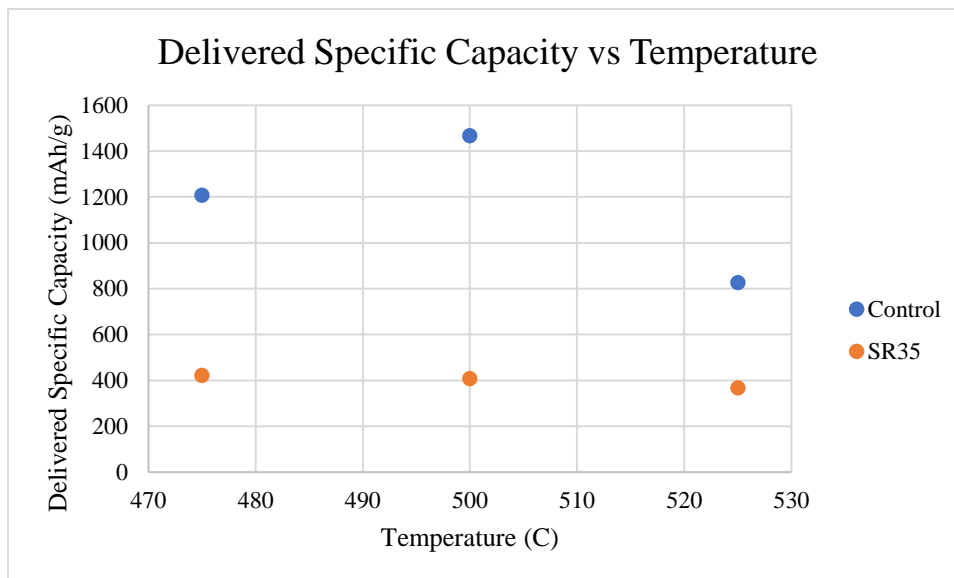


Figure 29. Delivered Specific Capacity (normalized by anode mass) vs Temperature for control and experimental cells at 475, 500, and 525C.

## Chapter 4 Conclusion and Future Work

### 4.1 Conclusion and Future Work

A new experimental thermal battery separator design has been presented and evaluated for feasibility at the single cell level. This experiment examined mechanical stability and electrochemical performance with respect to the existing pellet technology. A finite element analysis, discharge testing, and electrical impedance spectroscopy have shown the experimental separator design functions as a proof of concept. However, there are many improvements that need to be made for a feasible design.

The finite element analysis performed in ABAQUS has shown the MACOR<sup>®</sup> ceramic can withstand loading conditions of a thermal battery environment. However, the experimental separator design merits much more rigorous investigation for any real application. The material should be characterized for yield criteria as a function of strain rate and temperature. The MACOR<sup>®</sup> ceramic should also be investigated for directionally dependent material properties. With more detailed material data, plasticity can then be incorporated into the FEA model and a much more accurate conclusion can be made about the material limits.

Electrical impedance spectroscopy was performed and analyzed to characterize impedance mechanisms at work in both the control and experimental separators. The data on the traditional pellet separators has been modeled with an equivalent circuit and fit with a high level of confidence as shown in Appendix A. Additional circuit elements were needed to fit the EIS data of the experimental cells. Sum of square and Chi-squared values begin to increase for these experimental cells due to an equivalent circuit that does not fully capture the impedance mechanisms. Possible contributions to the fitting deviations may be due to material reactivity, geometric influences, and electrolyte leakage.

In addition to possible issues between the electrolyte and MACOR<sup>®</sup> ceramic, the experimental separator design may only be ideal for certain electrodes. Preliminary testing with a pellet LiSi anode proved to be highly soluble when in contact with the LiCl-KCl electrolyte of the experimental cells. Alternatively, a LiB foil was chosen for the anode during single cell testing. The experimental cells delivered less than half of the specific

capacity compared to cells with a traditional pellet separator. Possible reasons for this include rapid Li consumption of the LiB anode, inhomogeneous current density through the experimental separator, and mechanical failures.

In conclusion, the alternative separator design has been demonstrated as a proof of concept. However, much more rigorous mechanical and electrochemical investigation is needed to be a feasible option in a real-world application. Alternative ceramic materials such as MgO and AlO<sub>2</sub> may also prove to have the desired mechanical robustness of MACOR<sup>®</sup> while remaining unreactive with LiCl-KCl electrolyte. Future work should also include incorporation of the experimental separator design into a full-scale battery build.

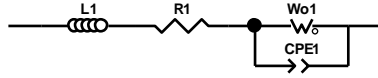
## References

- <sup>1</sup>Guidotti, R., & Masset, P. (2006, July 25). Thermally activated ("thermal") battery technology: Part i: An overview.
- <sup>2</sup>“Masset, P., & Guidotti, R. (2006, December 01). Thermal activated (thermal) battery technology: Part ii. molten salt electrolytes..
- <sup>3</sup> (n.d.). Retrieved from [http://www.asb-group.com/sites/default/files/FICHE-9-GB\\_ASB.pdf](http://www.asb-group.com/sites/default/files/FICHE-9-GB_ASB.pdf)
- <sup>4</sup> Guidotti, R., & Reinhardt, W. (1996, September 01). Characterization of mgo powders for use in thermal batteries.
- <sup>5</sup> Masset, P., Schoeffert, S., Poinso, J., & Poignet, J. (2004, September 08). Retained molten salt electrolytes in thermal batteries.
- <sup>6</sup> Guidotti, R., & Reinhardt, F. (1999, September 08). Evaluation of fiber separators for use in thermal batteries.
- <sup>7</sup>Reinhardt, F., & Guidotti, R. (2006, June 01). Evaluation of ceramic papers and tapes for use as separators in thermal batteries.
- <sup>8</sup> Kuper, W. E. (1994). *36th Power Sources Conference* (pp. 300-310). Cherry Hill, New Jersey: U.S. Army Research Laboratory.  
doi:<https://apps.dtic.mil/dtic/tr/fulltext/u2/a281443.pdf>
- <sup>9</sup> Mondy, L., Roberts, C., Grillet, A., Soehnel, M., Barringer, D., DiAntonio, C., . . . Fitchett, S. (2013, November 01). New composite separator pellet to increase power density and reduce size of thermal batteries.
- <sup>10</sup> Long, K., Roberts, C., Roberts, S., & Grillet, A. (2014, June 01). The mechanics of pressed-pellet separators in molten salt batteries.
- <sup>11</sup> Roberts, S. A., Jove-Colon, C. F., Moffat, H. K., Neilsen, M. L., Piekos, E. S., Schroeder, B. B., . . . Voskuilen, T. G. (n.d.). *TABS: A Thermal Battery Desktop Design Tool* (Tech.). Retrieved <http://people.cs.ksu.edu/~neilsen/papers/2018/TABS29-4.pdf>
- <sup>12</sup> Guidotti, R., Reinhardt, F., & Thomas, E. (2015, September 12). A study of the stack relaxation in thermal batteries on activation.
- <sup>13</sup> Bäker, M. (n.d.). How to get meaningful and correct results from your finite element model.

- <sup>14</sup> Callister, W. D., & Rethwisch, D. G. (2020). Materials science and engineering: An introduction. In *Materials science and engineering: An introduction* (pp. 485-486). Hoboken, NJ: Wiley.
- <sup>15</sup> Danzer, R. (2014, June 23). On the relationship between ceramic strength and the requirements for mechanical design.
- <sup>16</sup> MACOR<sup>®</sup> Machinable Glass Ceramic for Industrial Applications, <https://www.corning.com/media/worldwide/csm/documents/71759a443535431395eb34ehead091cb.pdf>
- <sup>17</sup> Shen, Y. -. (2010). *Constrained deformation of materials: Devices, heterogeneous structures and thermo-mechanical modeling*. New York: Springer.
- <sup>18</sup> Khraishi, T. A., & Shen, Y. (n.d.). *Introductory Continuum Mechanics*. San Diego, California: Congella.
- <sup>19</sup> Huang, J. (2018, May 24). Diffusion impedance OF electroactive materials, Electrolytic solutions and porous electrodes: Warburg impedance and beyond.
- <sup>20</sup> Hamann, C. H., Hamnett, A., & Vielstich, W. (2007). *Electrochemistry*. Weinheim: Wiley-VCH-Verl.
- <sup>21</sup> M S Meikhall *et al* (1993). *J. Phys. D: Appl. Phys.* **26** 1125
- <sup>22</sup> S. D.. James, L., L. E.. Vries, L., R.. Szwarc, R., R.. Szwarc, R., James, S., R.. Szwarc, S., . . . R. A.. Sharma, R. (1976, January 01). Preparation and characterization of lithium-boron alloys: Electrochemical studies as anodes in molten salt media, and comparison with pure lithium-involving systems.

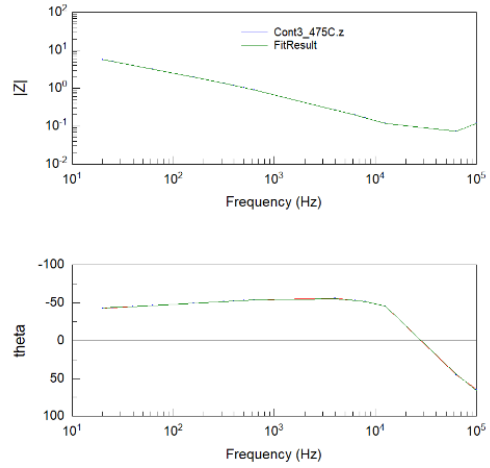
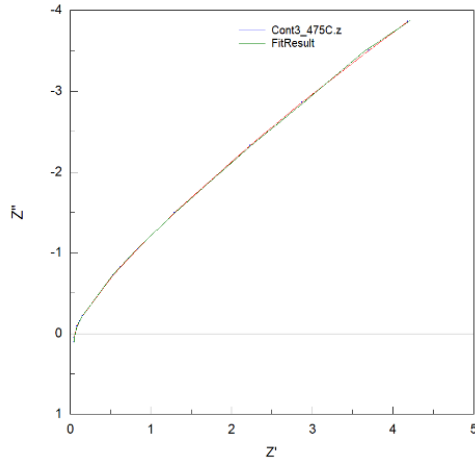
# Appendix

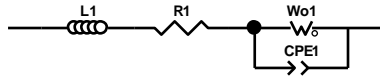
## A. Electrical Impedance Data



Element	Freedom	Value	Error	Error %
L1	Free(+)	2.0182E-07	1.105E-09	0.54752
R1	Free(+)	0.041995	0.00067377	1.6044
Wo1-R	Free(+)	198.1	13.602	6.8662
Wo1-T	Free(+)	0.074604	0.0034992	4.6904
Wo1-P	Free(+)	0.84221	0.0090864	1.0789
CPE1-T	Free(+)	0.02133	0.00046625	2.1859
CPE1-P	Free(+)	0.40489	0.0067109	1.6575

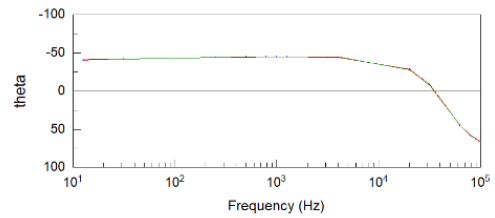
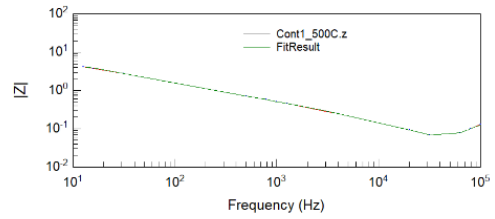
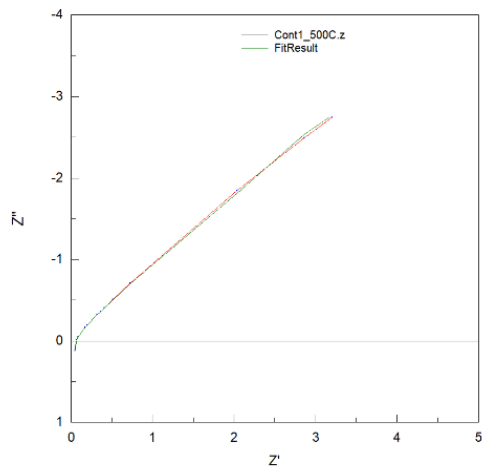
Chi-Squared: 4.7873E-05  
 Weighted Sum of Squares: 0.0011011

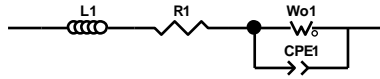




Element	Freedom	Value	Error	Error %
L1	Free(+)	2.2656E-07	1.4911E-09	0.65815
R1	Free(+)	0.038926	0.00079128	2.0328
Wo1-R	Free(+)	349	13.338	3.8218
Wo1-T	Fixed(X)	0.036478	N/A	N/A
Wo1-P	Fixed(X)	0.90206	N/A	N/A
CPE1-T	Free(+)	0.031375	0.00042595	1.3576
CPE1-P	Free(+)	0.4599	0.0022589	0.49117

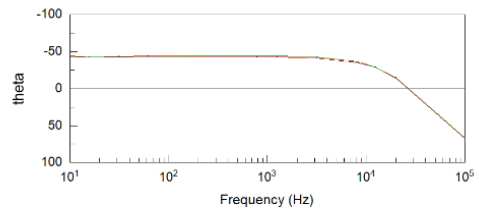
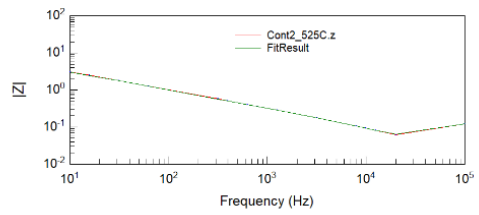
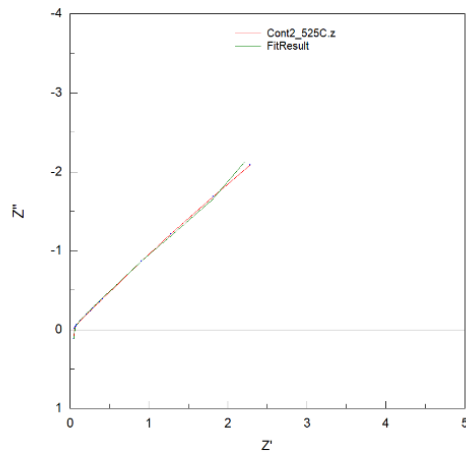
Chi-Squared: 9.2913E-05  
 Weighted Sum of Squares: 0.0023228

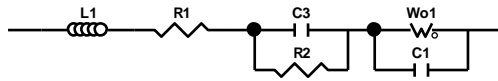




Element	Freedom	Value	Error	Error %
L1	Free(+)	1.9703E-07	3.4962E-09	1.7745
R1	Free(+)	0.043145	0.0013886	3.2184
Wo1-R	Free(+)	609.5	60.558	9.9357
Wo1-T	Free(+)	0.067867	0.00222	3.2711
Wo1-P	Free(+)	0.98623	0.0092055	0.9334
CPE1-T	Free(+)	0.046889	0.0014218	3.0323
CPE1-P	Free(+)	0.47492	0.0051754	1.0897

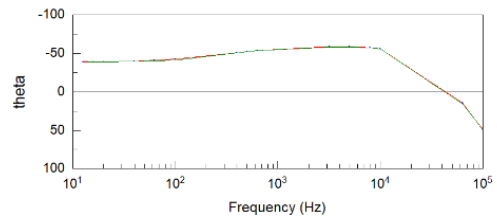
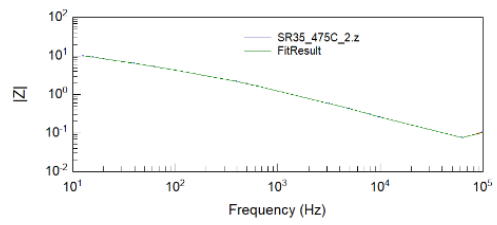
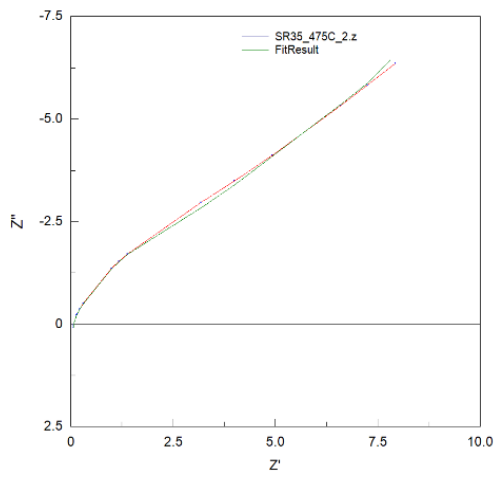
Chi-Squared: 0.00029847  
 Weighted Sum of Squares: 0.0068647

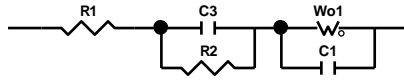




Element	Freedom	Value	Error	Error %
L1	Free(+)	1.7677E-07	1.6725E-09	0.94614
R1	Free(+)	0.063579	0.00074976	1.1793
C3	Free(+)	0.00077262	3.578E-05	4.631
R2	Free(+)	0.87385	0.048285	5.5255
Wo1-R	Free(+)	25	0.21485	0.8594
Wo1-T	Fixed(X)	0.087641	N/A	N/A
Wo1-P	Fixed(X)	0.46776	N/A	N/A
C1	Free(+)	4.3267E-05	6.9734E-07	1.6117

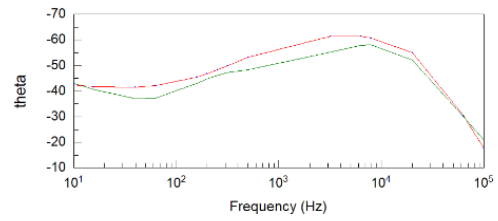
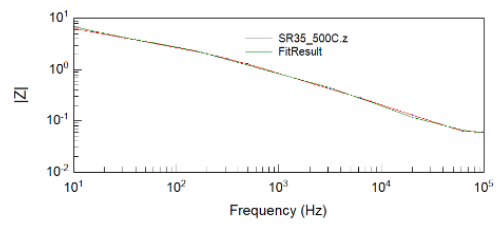
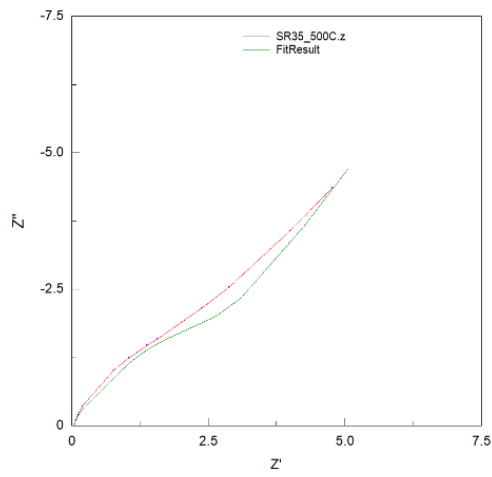
Chi-Squared: 0.00012794  
 Weighted Sum of Squares: 0.0030705

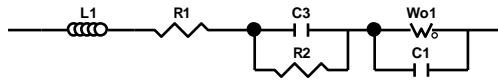




Element	Freedom	Value	Error	Error %
R1	Free(+)	0.052795	0.0022278	4.2197
C3	Free(+)	0.00091522	8.0134E-05	8.7557
R2	Free(+)	1.191	0.10544	8.8531
Wo1-R	Fixed(X)	2.016	N/A	N/A
Wo1-T	Fixed(X)	0.0028234	N/A	N/A
Wo1-P	Fixed(X)	0.30189	N/A	N/A
C1	Free(+)	7.9309E-05	3.6858E-06	4.6474

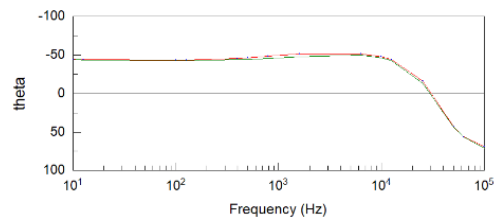
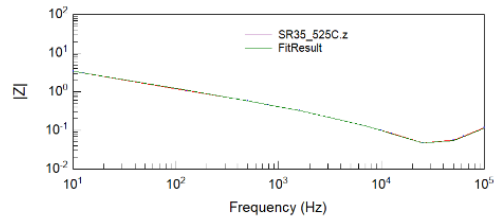
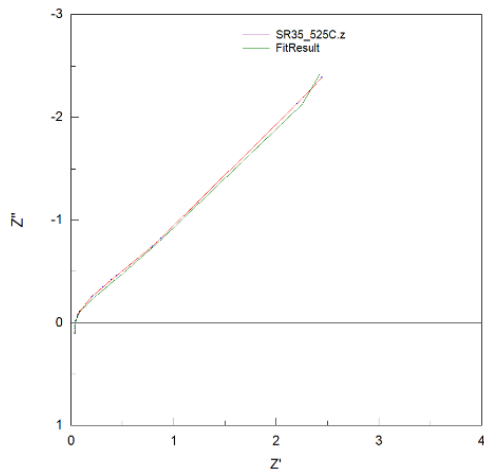
Chi-Squared: 0.0030403  
 Weighted Sum of Squares: 0.079048

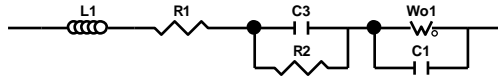




Element	Freedom	Value	Error	Error %
L1	Free(+)	1.9077E-07	3.2272E-09	1.6917
R1	Free(+)	0.035428	0.00095638	2.6995
C3	Free(+)	0.006372	0.00092554	14.525
R2	Free(+)	0.68843	0.087001	12.638
Wo1-R	Free(+)	2.807	0.062805	2.2374
Wo1-T	Fixed(X)	0.019825	N/A	N/A
Wo1-P	Fixed(X)	0.37528	N/A	N/A
C1	Free(+)	0.00012288	3.7611E-06	3.0608

Chi-Squared: 0.00082255  
 Weighted Sum of Squares: 0.019741

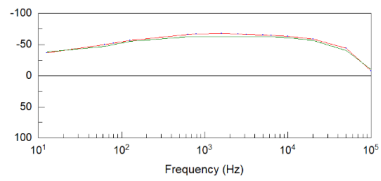
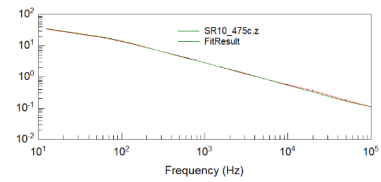
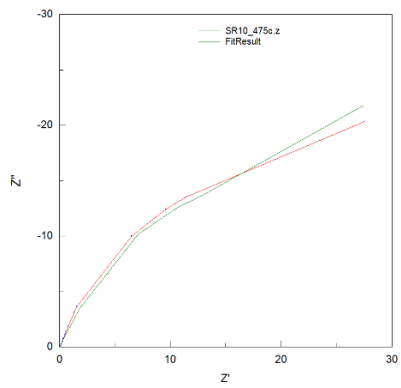




Element	Freedom	Value	Error	Error %
L1	Free(+)	8.6618E-08	1.1467E-08	13.239
R1	Free(+)	0.094183	0.0058448	6.2058
C3	Free(+)	0.00022093	3.2226E-05	14.587
R2	Free(+)	10.39	1.6466	15.848
Wo1-R	Free(+)	437.6	33.226	7.5928
Wo1-T	Fixed(X)	2.405	N/A	N/A
Wo1-P	Fixed(X)	0.52951	N/A	N/A
C1	Free( $\pm$ )	1.8044E-05	1.5146E-06	8.3939

Chi-Squared: 0.0029235

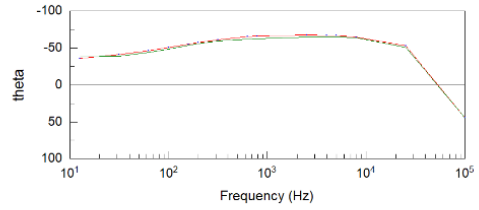
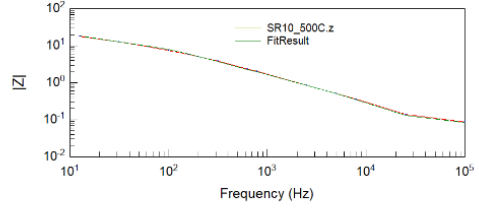
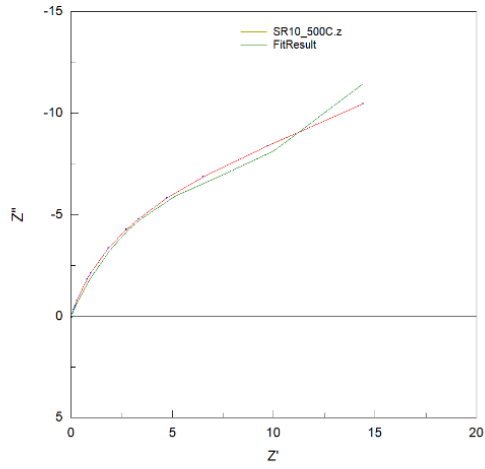
Weighted Sum of Squares: 0.070164





Element	Freedom	Value	Error	Error %
L1	Free(+)	1.5083E-07	5.6641E-09	3.7553
R1	Free(+)	0.056112	0.0029681	5.2896
C3	Free(+)	0.00040569	4.1443E-05	10.215
R2	Free(+)	4.27	0.52613	12.322
Wo1-R	Free(+)	759.6	39.861	5.2476
Wo1-T	Fixed(X)	30.88	N/A	N/A
Wo1-P	Fixed(X)	0.49973	N/A	N/A
C1	Free(±)	4.2071E-05	1.951E-06	4.6374

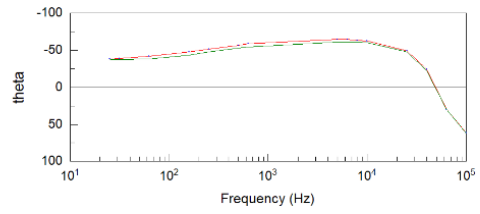
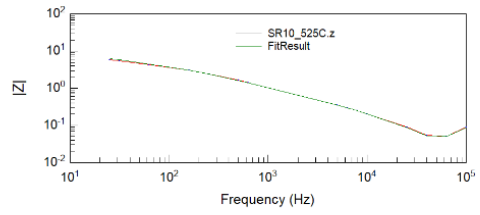
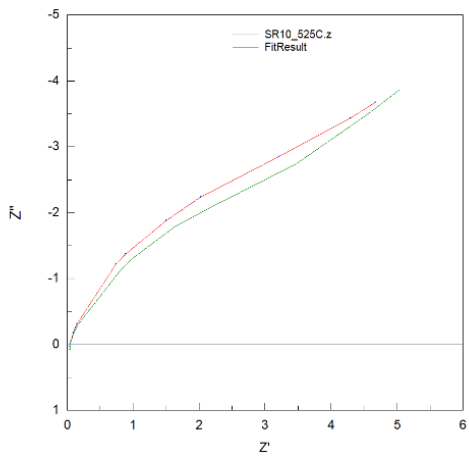
Chi-Squared: 0.0015354  
 Weighted Sum of Squares: 0.036849





Element	Freedom	Value	Error	Error %
L1	Free(+)	1.6411E-07	4.9317E-09	3.0051
R1	Free(+)	0.036695	0.0016287	4.4385
C3	Free(+)	0.0008049	9.8154E-05	12.195
R2	Free(+)	0.96202	0.10915	11.346
W01-R	Fixed(X)	354.7	N/A	N/A
W01-T	Fixed(X)	59.17	N/A	N/A
W01-P	Fixed(X)	0.45183	N/A	N/A
C1	Free(±)	5.5662E-05	2.5229E-06	4.5325

Chi-Squared: 0.0020588  
 Weighted Sum of Squares: 0.05147



## B. Discharge Data

